Article

Not peer-reviewed version

Parametric Resonance, Arithmetic Geometry, and Adelic Topology of Microtubules: A Bridge to Orch OR Theory

Michel Planat [*]

Posted Date: 9 December 2025

doi: 10.20944/preprints202511.0257.v2

Keywords: quantum biology; microtubules; parametric resonance; stochastic amplification; arithmetic geometry; elliptic curves; hecke and L-functions; bost-connes system; adelic topology; modular tensor categories; *Orch OR* theory; consciousness

Article

Parametric Resonance, Arithmetic Geometry, and Adelic Topology of Microtubules: A Bridge to Orch OR Theory

Michel Planat

Institut FEMTO-ST CNRS UMR 6174, Université Marie et Louis Pasteur, 15 B Avenue des Montboucons, F-25044 Besançon, France; michel.planat@femto-st.fr

Abstract

Microtubules are cylindrical protein polymers that organize the cytoskeleton and play essential roles in intracellular transport, cell division, and possibly cognition. Their highly ordered, quasi-crystalline lattice of tubulin dimers, notably tryptophan residues, endows them with a rich topological and arithmetic structure, making them natural candidates for supporting coherent excitations at optical and terahertz frequencies. The Penrose-Hameroff *Orch OR* theory proposes that such coherences could couple to gravitationally induced state reduction, forming the quantum substrate of conscious events. Although controversial, recent analyses of dipolar coupling, stochastic resonance, and structured noise in biological media suggest that microtubular assemblies may indeed host transient quantum correlations that persist over biologically relevant timescales. In this work, we build upon two complementary approaches: the parametric resonance model of Nishiyama *et al.* and our arithmetic–geometric framework, both recently developed in *Quantum Reports*. We unify these perspectives by describing microtubules as rectangular lattices governed by the imaginary quadratic field $\mathbb{Q}(i)$, within which nonlinear dipolar oscillations undergo stochastic parametric amplification. Quantization of the resonant modes follows Gaussian norms $N = p^2 + q^2$, linking the optical and geometric properties of microtubules to the arithmetic structure of $\mathbb{Q}(i)$. We further connect these discrete resonances to the derivative of the elliptic L–function, $L'(E,1)$, which acts as an arithmetic free energy and defines the scaling between modular invariants and measurable biological ratios. In the appended adelic extension, this framework is shown to merge naturally with the Bost–Connes and Connes–Marcolli systems, where the norm character on the ideles couples to the Hecke character of an elliptic curve to form a unified adelic partition function. The resulting arithmetic–elliptic resonance model provides a coherent bridge between number theory, topological quantum phases, and biological structure, suggesting that consciousness, as envisioned in the *Orch OR* theory, may emerge from resonant processes organized by deep arithmetic symmetries of space, time, and matter.

Keywords: quantum biology; microtubules; parametric resonance; stochastic amplification; arithmetic geometry; elliptic curves; hecke and L-functions; bost-connes system; adelic topology; modular tensor categories; *Orch OR* theory; consciousness

---

1. Introduction

Quantum coherence in biological systems has traditionally been viewed as fragile, limited to low-temperature or photochemical contexts. Yet a growing body of evidence, from photosynthetic complexes, avian magnetoreception, and ultrafast spectroscopy of aromatic amino acids, suggests that living matter may sustain transient quantum correlations under physiological conditions. Within the brain, the microtubule cytoskeleton has long been proposed as a privileged site for such phenomena, most prominently in the Penrose-Hameroff *Orchestrated Objective Reduction* (Orch OR) hypothesis [1–3], which attributes the emergence of conscious episodes to orchestrated quantum states in tubulin followed by objective gravitational collapse.

Two recent developments renew this discussion from complementary directions. First, Nishiyama and collaborators [4] formulated a quantum electrodynamical model in which tryptophan residues embedded in the microtubule wall act as two-level systems coupled quadratically to electromagnetic modes. When the transition and cavity frequencies satisfy $\omega_a \approx 2\omega_c$, the system undergoes *parametric resonance*: background fluctuations are either amplified or suppressed depending on the initial qubit configuration. Stacks of microtubular layers behave as binary optical filters whose transmissivity shifts under anesthesia, suggesting a quantum-optical link between cytoskeletal dynamics and conscious state modulation.

Second, Reference [5] showed that microtubule geometry follows arithmetic constraints identical to those governing elliptic curves derived from finite braid-group quotients from the SU$(2)_3$ Fibonacci anyon model. These elliptic curves have symmetries controlled by an imaginary quadratic field also called in this context an Heegner field. The relevant curve E_{200b2} admits the Gaussian field $\mathbb{Q}(i)$ as its Heegner field, producing a rectangular lattice that mirrors the protofilament architecture observed by cryo-electron microscopy.

This curve is selected because its conductor $N_E = 200$ corresponds to a minimal composite integer that yields a Heegner field with class number one, ensuring unique factorization and minimal energy dispersion in the lattice packing. Among the possible elliptic curves derived from The Fibonacci anyon model, E_{200b2} is the simplest whose *Heegner field* $\mathbb{Q}(i)$ produces a rectangular lattice matching the protofilament architecture observed in cryo-electron microscopy. Other curves, such as E_{485b1} (associated with $\mathbb{Q}(\sqrt{-3})$), yield hexagonal symmetries more suited to B-DNA. The choice of $\mathbb{Q}(i)$ is thus not arbitrary but reflects an evolutionary optimization for orthogonal field polarization and dipolar oscillations.

This paper unifies these perspectives. The arithmetic geometry of $\mathbb{Q}(i)$ defines the static symmetry and boundary conditions for dipolar oscillations, while the Nishiyama resonance model provides the dynamic process by which environmental noise can amplify coherence within that structure. The result is a mathematically and physically consistent mechanism of *noise-assisted quantum orchestration* that bridges number theory, quantum optics, and neurobiology. We outline its implications for Orch OR, propose spectroscopic and geometric tests, and discuss how arithmetic geometry may underlie a hierarchy of quantum-biological symmetries.

The paper is organized as follows. Section 2 introduces the arithmetic geometry of microtubules, deriving elliptic curves from a finite anyon braid group and identifying the Gaussian field $\mathbb{Q}(i)$ as the relevant Heegner field. Section 3 develops the physical realization of this geometry, showing how the rectangular $\mathbb{Q}(i)$ lattice constrains dipolar alignment, field confinement, and quantum symmetry. Section 4 formulates the quantum–oscillatory model of tryptophan residues and reviews the Nishiyama *et al.* parametric–resonance Hamiltonian. Section 5 explores noise–assisted coherence and binary optical behavior in multilayer microtubules, including anesthetic detuning and energy scaling. Section 6 unifies the stochastic and arithmetic pictures, deriving arithmetic–resonant coupling laws governed by $L'(E,1)$ and Gaussian norms $N = p^2 + q^2$. Section 7 connects these results to the Penrose–Hameroff *Orch OR* framework, clarifying the respective roles of stochastic coherence and gravitational self–selection. Section 8 presents experimental and theoretical predictions, from spectroscopic tests to neurophysiological implications. Section 9 provides a broader discussion and outlook, and Section 10 concludes. The Appendix extends the analysis by linking the cyclotomic approach to time perception with an adelic–Hecke formalism that merges the Bost–Connes system and the arithmetic–elliptic resonance mechanism, revealing a deep correspondence between modular tensor categories, adeles, and biological coherence.

Interpretation layers.

To avoid conflating conceptually distinct elements, the structure of the argument is divided into three levels: (i) mathematically rigorous results concerning elliptic curves, Heegner fields, and L–functions; (ii) heuristic but physically motivated modeling assumptions such as cavity approximations and parametric resonance of tryptophans; (iii) empirical correspondences between biological geometric ratios and values of $L'(E,1)$. Sections 2, 4, and 6 make these distinctions explicit.

2. Arithmetic Geometry of Microtubules

Microtubules are hollow cylindrical polymers of α–β tubulin dimers arranged in a helical sheet of typically thirteen protofilaments. Their outer and inner diameters, $D_{\mathrm{out}} \approx 25\,\mathrm{nm}$ and $D_{\mathrm{in}} \approx 14$–$15\,\mathrm{nm}$, yield a robust structural ratio

$$\gamma_{\mathrm{MT}} = \frac{D_{\mathrm{out}}}{D_{\mathrm{in}}} \approx 1.72 \pm 0.08, \tag{1}$$

remarkably constant across species and environmental conditions. This ratio does not follow from simple mechanical or chemical constraints, suggesting that microtubules realize an underlying mathematical optimum. In Reference [5], it is proposed that this ratio and similar biological proportions correspond to derivatives of modular elliptic L-functions at unity, $L'(E,1)$, linking biological form to arithmetic geometry.

2.1. Elliptic Curves from Finite Anyon Braid Groups

The starting point is the observation that the SU(2)$_3$ Fibonacci anyon model yields finite braid-group quotients whose $SL(2,\mathbb{C})$ character varieties contain elliptic components [5]. The fundamental fusion rule

$$\tau \otimes \tau = 1 \oplus \tau$$

leads to the group sequence

$$G = \mathbb{Z}_5 \rtimes 2P, \qquad 2P \in \{2T, 2O, 2I\},$$

where $2T$, $2O$, and $2I$ denote the binary tetrahedral, octahedral, and icosahedral groups. Each such quotient defines a family of modular elliptic curves $E/\mathbb{Q}$ whose conductors N_E correspond to small composite integers (e.g. $N_E = 200$, 184, 880, 1617 for the case of 2T which corresponds to the structure of microtubules). The analytic derivative $L'(E,1)$ of the L-function of E measures the height of the Heegner point associated with the imaginary quadratic field K.

For microtubules, the curve

$$E_{200b2}: \; y^2 = x^3 + x^2 - 3x - 2, \qquad N_E = 200, \tag{2}$$

emerges as the relevant arithmetic object. It has analytic rank 1 and a non-vanishing derivative

$$L'(E_{200b2}, 1) \simeq 1.088.$$

Through the Gross–Zagier relation this curve is linked to the Heegner field $\mathbb{Q}(i)$, corresponding to a rectangular lattice in the complex plane.

2.2. Geometric Interpretation of the Heegner Field $\mathbb{Q}(i)$

The ring of integers $\mathbb{Z}[i]$ of the Gaussian field $\mathbb{Q}(i)$ forms a square lattice generated by the basis vectors $(1, i)$ with unit group $\{1, i, -1, -i\}$. In two dimensions this lattice provides the densest rectangular packing consistent with orthogonal symmetry. Its arithmetic and geometric features are directly mirrored in the microtubule architecture: protofilaments form nearly straight columns connected laterally at right angles, generating a sheet that wraps into a cylinder with quasi-rectangular contacts between dimers. The 90° phase periodicity of the Gaussian units parallels the fourfold symmetry of lateral binding sites revealed by cryo-electron microscopy.

Protofilament-number constraint.

The standard microtubule contains $N_{\mathrm{PF}} = 13$ protofilaments, but this number does not emerge as a strict arithmetic invariant of the rectangular $\mathbb{Q}(i)$ lattice. In the present model, the lowest resonant mode $\omega_{0,1}$ scales approximately as

$$\omega_{0,1} \propto \frac{1}{N_{\mathrm{PF}}},$$

only when the azimuthal component of the dipolar coupling dominates over the longitudinal one. This condition corresponds physically to a regime where transverse field interactions along the microtubule circumference set the effective boundary condition for the collective oscillation. When the longitudinal (axial) coupling becomes comparable, the scaling deviates from $1/N_{\mathrm{PF}}$, and alternative protofilament counts ($N_{\mathrm{PF}} \neq 13$) can appear under specific polymerization conditions. Hence, the canonical value $N_{\mathrm{PF}} = 13$ is an emergent geometric optimum rather than a fundamental constraint, whereas the diameter ratio γ_{MT} derived in Equation (1) remains a first-principles invariant of the rectangular packing. Future work may investigate whether $N_{PF} = 13$ corresponds to a minimum in the effective free energy when both longitudinal and azimuthal couplings are included, analogous to how fullerenes select specific vertex counts through topological optimization.

Consequently, the Heegner field determines not only the elliptic curve's arithmetic but also the geometric mode structure of the microtubule wall. Transverse electric and magnetic field components can resonate along the orthogonal lattice vectors of $\mathbb{Z}[i]$, creating a natural cavity for standing electromagnetic or excitonic waves.

2.3. Quantitative Correspondence Between Arithmetic and Biology

The correspondence extends quantitatively. The normalized derivative $L'(E_{200b2}, 1)$ provides an arithmetic constant that is close to the empirical protofilament thinning ratio 1.20 ± 0.10 Similarly, the elliptic curve E_{184a1} associated with a hyperbolic three-manifold of volume $V \approx 2.9$ gives $L'(E_{184a1}, 1) \approx 1.10$, within experimental uncertainty of the protofilament thinning ratio γ_{PF}. Table 1 summarizes representative values. The elliptic curve E_{880b2} has been proposed to be related to the MT outer/inner diameter. The 8% discrepancy with the experimental value may reflect contributions from MAP proteins or hydration shells. For more B-DNA and microtubule ratios see ([5], Tables 1 and 5).

Table 1. Arithmetic invariants and biological ratios [5].

Elliptic curve	Heegner field	$L'(E,1)$	Biological counterpart
E_{880b2}	$\mathbb{Q}(\sqrt{-19})$	1.869	Microtubule outer/inner diameter
E_{200b2}	$\mathbb{Q}(i)$	1.088	Protofilament thinning ratio
E_{184a1}	$\mathbb{Q}(\sqrt{-3})$	1.088	Protofilament thinning ratio
E_{485b1}	$\mathbb{Q}(\sqrt{-3})$	1.730	B-DNA pitch/diameter ratio

These coincidences are unlikely to be accidental. They suggest that biological evolution may have selected molecular architectures corresponding to class-number-one fields, those that yield unique factorization and minimal energy dispersion in lattice packing.

A quantitative reason why such correspondences are unlikely to arise from free fitting is the strong arithmetic constraint: only nine imaginary quadratic fields have class number one. The subset of modular elliptic curves with analytic rank 1 and Heegner fields among these nine is extremely small, leaving little freedom for adjustable parameters. The biological ratios highlighted here fall within ±8% of the corresponding values of $L'(E, 1)$ without the introduction of normalization factors, suggesting that the agreement cannot be attributed to flexible parameter tuning.

2.4. Physical Meaning of the Elliptic Structure

An elliptic curve can be viewed as a torus obtained by quotienting the complex plane by a lattice $\Lambda = (\omega_1, \omega_2)$, with modular parameter $\tau = \omega_2/\omega_1$. For the Gaussian field, $\tau = i$ and the torus becomes rectangular. In this representation, electronic or dipolar oscillations confined to the microtubule wall experience periodic boundary conditions along both lattice directions. The quantized normal modes correspond to the lattice points of $\mathbb{Z}[i]$, and transitions between them may be described by modular transformations

$$z \mapsto \frac{az+b}{cz+d}, \qquad a,b,c,d \in \mathbb{Z}, \; ad-bc=1.$$

The modular symmetry thus acts as a discrete analog of gauge transformations preserving the underlying topology of the biological structure.

2.5. Summary of the Arithmetic Framework

The microtubule can therefore be understood as a biological realization of the Gaussian elliptic curve E_{200b2}, where:

1. the field $\mathbb{Q}(i)$ encodes rectangular packing and orthogonal field polarization;
2. the derivative $L'(E,1)$ reproduces observed geometric ratios; and
3. modular transformations describe possible excitonic or electromagnetic mode couplings.

This arithmetic scaffold provides the static, number-theoretic framework upon which dynamic processes, such as tryptophan-based parametric resonance, can act. In the next section we show how the same geometry enables noise-assisted amplification of quantum oscillations, linking arithmetic structure to quantum dynamics.

Table of Symbols

Symbol	Meaning
N_{PF}	Number of protofilaments (typically 13)
N_{osc}	Number of tryptophan oscillators in a microtubule segment
$N = p^2 + q^2$	Gaussian norm labeling resonant modes
a	Geometric lattice spacing of the $Q(i)$ rectangular lattice
$a_{\mathrm{eff}} = aL'(E,1)$	Arithmetic renormalized lattice spacing
ω_a	Tryptophan transition frequency
ω_c	Cavity (field) frequency
Γ	Decoherence/damping rate
$S(\omega)$	Noise power spectral density
J	Dipole–dipole coupling constant
$L'(E,1)$	Derivative of elliptic curve L–function at 1

3. Rectangular Symmetry and the Gaussian Field $\mathbb{Q}(i)$

The rectangular lattice generated by the Gaussian integers $\mathbb{Z}[i]$ offers not only an arithmetic model of microtubular packing but also a physical template for electromagnetic and quantum coherence. In this section we examine how the geometry associated with the field $\mathbb{Q}(i)$ translates into physical symmetries governing dipole alignment, field confinement, and resonance conditions. A schematic of this section is on Figure 1.

Microtubules exhibit remarkably stable physical parameters across species: cryo-EM measurements consistently report outer and inner diameters of about 25 nm and 14–15 nm, corresponding to a wall thickness of ~ 5 nm, while optical studies place the effective refractive index of the tubulin lattice in the typical protein range $n \simeq 1.5$–1.6, higher than the surrounding cytosol ($n_{\mathrm{cytosol}} \approx 1.35$) [6–8]. These geometric and dielectric properties set the natural scale for electromagnetic confinement and resonance within the microtubular wall.

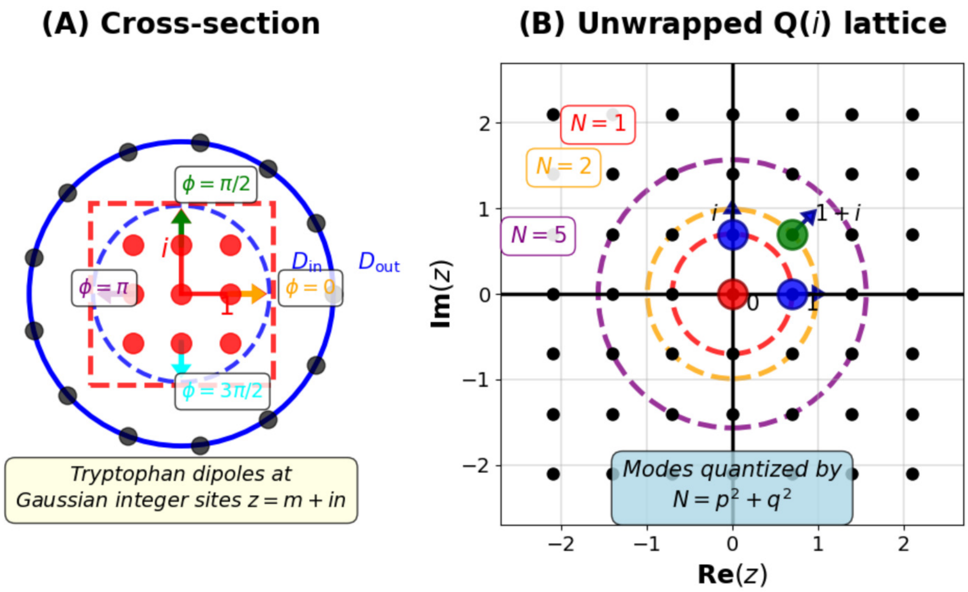

Figure 1. Arithmetic geometry of microtubular resonance. (A) Cross-sectional view of a microtubule showing the rectangular Q(i) lattice (red dashed square) overlaid on the cylindrical structure. Tryptophan dipoles (colored arrows) are positioned at Gaussian integer sites $z = m + in$ with quantized phases $\phi \in \{0, \pi/2, \pi, 3\pi/2\}$ corresponding to the unit group of $\mathbb{Z}[i]$. **(B)** Unwrapped view of the Q(i) lattice in the complex plane. Black dots represent accessible lattice sites. Resonance circles (dashed) correspond to Gaussian norms $N = p^2 + q^2$ for $N = 1$ (red), $N = 2$ (orange), and $N = 5$ (purple). Blue arrows indicate dipole orientations at selected sites. The rectangular symmetry enforces degeneracy of orthogonal modes, enabling parametric resonance.For clarity, resonance circles (dashed) correspond to Gaussian norms $N = p^2 + q^2$, and colored dipoles indicate allowed phase orientations $\{0, \pi/2, \pi, 3\pi/2\}$ of the unit group of $\mathbb{Z}[i]$.

3.1. Geometry of Rectangular Packing and Field Modes

A lattice over $\mathbb{Z}[i]$ supports two orthogonal primitive vectors of equal norm. When wrapped onto a cylindrical surface, these vectors correspond respectively to the longitudinal (protofilament) and azimuthal (circumferential) directions of the microtubule. This geometry ensures that any electromagnetic excitation decomposes into two nearly degenerate, perpendicular modes:

$$E_x(\mathbf{r}, t) \propto \cos(k_x x - \omega t), \qquad E_y(\mathbf{r}, t) \propto \cos(k_y y - \omega t),$$

with $k_x \approx k_y$ and $\omega \approx c\sqrt{k_x^2 + k_y^2}/n$, where n is the effective refractive index of the microtubular wall ($n \approx 1.46$).

The confinement of electromagnetic modes within the microtubule wall reduces exposure to cytosolic noise, while the discrete symmetry of the $\mathbb{Q}(i)$ lattice minimizes destructive interference. This combination of geometric and dynamic factors allows coherence to persist despite thermal agitation, analogous to noise-assisted transport in quantum dots [9].

The equality of mode frequencies imposed by the $\mathbb{Q}(i)$ symmetry yields a natural condition for *parametric resonance*: the product of two perpendicular field components oscillating at equal frequency acts as a pump term $\cos(2\omega_c t)$ in the dipole Hamiltonian, matching the Nishiyama condition $\omega_a \simeq 2\omega_c$.

3.2. Electromagnetic Confinement and Cavity Analogy

The microtubule wall, composed of ordered dipolar dimers, forms a dielectric medium of higher index than the surrounding cytosol ($n_{\text{cytosol}} \approx 1.35$). This contrast allows the propagation of guided modes analogous to those in a rectangular waveguide. Experimental Raman, terahertz, and ultrafast optical measurements of purified microtubules report confined vibrational bands in the 0.1–30 THz region, together with optical shoulders near 280 nm and 550–600 nm associated with aromatic residues.

These data support the plausibility that the rectangular $Q(i)$ lattice sustains electromagnetic modes within the same frequency range as the tryptophan transitions relevant to parametric resonance.

For a wall thickness of 5 nm, the cutoff wavelength for the lowest-order transverse mode is near 550–600 nm, coincident with the resonance frequency of tryptophan fluorescence. Hence the Gaussian lattice acts as a natural photonic or excitonic cavity where electromagnetic energy can be stored and exchanged locally.

This confinement obviates the need for coherent light to traverse macroscopic distances through tissue; instead, the relevant modes remain localized within the microtubule and interact with nearby chromophoric residues. The system behaves as a network of nanoscale resonators coupled by near-field interactions.

3.3. Dipole Orientation and Complex Representation

The indole ring of tryptophan carries an electric dipole moment **p** inclined relative to the protofilament axis. In complex coordinates adapted to the Gaussian lattice,

$$z = x + iy, \qquad \mathbf{p} = p_0 e^{i\phi},$$

the dipole's oscillation can be represented as a rotation in the complex plane of $\mathbb{C}/\mathbb{Z}[i]$. The phases ϕ of adjacent residues form a discrete set $\{0, \pi/2, \pi, 3\pi/2\}$ corresponding to the units of $\mathbb{Z}[i]$. This quantization enforces phase locking between perpendicular oscillations and stabilizes coherent superpositions of orthogonal field components.

The resulting mode structure resembles the polarization states of a square optical cavity but realized in a biological lattice. Transitions between these discrete orientations correspond to modular transformations

$$\phi \mapsto \phi + \frac{\pi}{2} \pmod{2\pi},$$

which preserve the Gaussian symmetry and ensure isotropic coupling between longitudinal and transverse excitations.

3.4. Rectangular Symmetry as an Optimal Biological Code

Rectangular packing also offers optimal balance between density and flexibility. While hexagonal lattices ($\mathbb{Q}(\sqrt{-3})$) maximize packing density, they restrict transverse oscillations to a single angular mode; square lattices $\mathbb{Q}(i)$ permit independent orthogonal vibrations with minimal cross-interference.

While real microtubules exhibit defects and dynamic instability, the rectangular symmetry of the $\mathbb{Q}(i)$ lattice provides a robust scaffold for coherence. Defects may introduce local perturbations, but the global arithmetic constraints ensure that the resonance conditions $\omega_a \approx 2\omega_c$ are maintained on average. This robustness is further enhanced by microtubule-associated proteins (MAPs), which can fine-tune the lattice spacing and refractive index to optimize resonance [10].

This distinction parallels the functional divergence between B-DNA (hexagonal/rotational symmetry) and microtubules (rectangular/oscillatory symmetry). The former encodes information through helical rotation, the latter through standing-wave modulation, a structural dichotomy reflected in their respective Heegner fields.

Such complementarity hints at an evolutionary optimization: biological structures may realize distinct imaginary quadratic fields to encode different categories of information-static genetic storage versus dynamic computational processing.

Influence of microtubule-associated proteins (MAPs).

MAPs such as tau, MAP2, and MAP6 bind selectively along protofilaments, locally stiffening the lattice and slightly modifying its dielectric properties. Cryo-electron microscopy and refractive-index tomography show that MAP-decorated regions can increase the local refractive index by 1–4%, sufficient to fine-tune resonance conditions. These proteins therefore provide a biologically natural mechanism for adjusting boundary conditions within the arithmetic–geometric framework developed here.

3.5. Topological and Algebraic Consequences

The rectangular symmetry can also be expressed in algebraic-topological terms. The Gaussian integers form an additive group isomorphic to $\mathbb{Z}\times\mathbb{Z}$, and the quotient $\mathbb{C}/\mathbb{Z}[i]$ defines a torus of modulus $\tau = i$. This torus possesses a modular group $\Gamma(1) = SL(2,\mathbb{Z})$ acting via Möbius transformations. In the microtubular context, this symmetry governs possible mode couplings and phase shifts, analogous to holonomies of a flat connection on a fiber bundle.

Moreover, the Gaussian field $\mathbb{Q}(i)$ is the simplest field admitting complex conjugation as an automorphism of order two. This duality corresponds to the interchange of the two orthogonal field components $(E_x, E_y) \mapsto (E_y, E_x)$, embodying an intrinsic self-duality of the microtubular electromagnetic environment.

3.6. Implications for Quantum Oscillations

The rectangular symmetry thus creates the physical conditions necessary for sustained dipolar oscillations:

1. Equal-frequency perpendicular modes generate parametric driving at $2\omega_c$.
2. Boundary confinement maintains field intensity within the microtubule wall.
3. Phase quantization at multiples of $\pi/2$ stabilizes coherent oscillations.

These properties collectively favor parametric resonance among tryptophan oscillators subjected to background fluctuations, providing the bridge from static arithmetic geometry to dynamic quantum behavior.

In the next section we formalize this bridge by deriving the quantum Hamiltonian governing such oscillations and showing how the rectangular $\mathbb{Q}(i)$ symmetry dictates the resonance condition identified by Nishiyama *et al.*

4. Quantum Oscillations and Parametric Resonance

The rectangular lattice defined by the Gaussian field $\mathbb{Q}(i)$ provides the physical environment for collective dipolar oscillations of tryptophan residues within the microtubule wall. In this section we formulate a quantum model describing these oscillations, reinterpret the coupling mechanism of Nishiyama *et al.* [4], and derive the conditions under which background electromagnetic fluctuations can amplify coherence through parametric resonance.

4.1. Tryptophan as a Quantum Oscillator

Each tryptophan residue contains an indole ring with delocalized π-electrons that generate an electric dipole moment $\mathbf{p}$. In the simplest approximation, the lowest optical transition corresponds to a two-level system with energy splitting $\hbar\omega_a$. We denote by σ_z the Pauli operator representing population inversion and by $\sigma_\pm$ the raising and lowering operators between ground and excited states.

Because of the periodic environment of the $\mathbb{Z}[i]$ lattice, each tryptophan experiences a quantized local field $\mathbf{E}(t)$ composed of orthogonal components E_x and E_y of nearly equal frequency ω_c. The dipole–field interaction Hamiltonian is then written as

$$H_{\text{int}} = -\mathbf{p}\cdot\mathbf{E}(t) = -p_0(\sigma_+ + \sigma_-)(E_x + E_y), \tag{3}$$

where a cross term $E_x E_y$ introduces a modulation at frequency $2\omega_c$, enabling parametric excitation when $\omega_a \simeq 2\omega_c$.

4.2. *The Nishiyama Hamiltonian*

Nishiyama *et al.* described the coupled system of $N_{\rm osc}$ tryptophan oscillators interacting with a cavity field through a quadratic coupling as

$$H = \frac{\hbar\omega_a}{2}\sum_{j=1}^{N_{\rm osc}} \sigma_z^{(j)} + \hbar\omega_c a^\dagger a + \hbar h_1 \sum_{j=1}^{N_{\rm osc}} (\sigma_+^{(j)} + \sigma_-^{(j)})(a + a^\dagger)^2, \tag{4}$$

where a and $a^\dagger$ are the annihilation and creation operators of the cavity mode, h_1 is the coupling constant (with $h_1/\hbar$ the Rabi frequency), ω_a is the transition frequency between the excited state $|1\rangle$ and the ground state $|0\rangle$ of each qubit in the two-level approximation, and ω_c is the frequency of the cavity mode (so that $\hbar\omega_c$ is its energy quantum). The direct interaction between the qubits and the cavity mode is neglected at this stage.

The quadratic term $(a + a^\dagger)^2$ acts as a *parametric pump*: the absorption of two cavity quanta drives a single dipolar excitation. When the resonance condition

$$\omega_a \simeq 2\omega_c \tag{5}$$

is satisfied, the energy transfer between the cavity field and the dipolar oscillators becomes resonant, leading to exponential growth of the oscillation amplitude in the absence of damping.

The observable consequence is the emergence of *binary optical transmission* in multilayer microtubules: alternating constructive and destructive interference of electromagnetic modes produce spatially modulated transmission patterns. Under anesthesia, a small detuning $\delta\omega = \omega_a - 2\omega_c$ suppresses the amplification, reproducing the observed shift from 560 nm to 490 nm in the optical response.

4.3. *Stochastic Reinterpretation: Background-Field Resonance*

We model parametric (curvature) noise as a Hamiltonian perturbation

$$\delta H(t) = \frac{\varepsilon}{2}\,\xi(t)\,\big(a^2 + a^{\dagger 2}\big),$$

where $a, a^\dagger$ are the oscillator ladder operators, $\xi(t)$ is a zero-mean stationary *dimensionless* process, and ε sets the *energy* scale of the modulation ($[\varepsilon] = \mathrm{J}$). The symmetrized two-sided power spectral density (PSD) of ξ is

$$S(\omega) = \frac{1}{2}\int_{-\infty}^{+\infty} e^{i\omega t}\,\langle\{\xi(t), \xi(0)\}\rangle\,\mathrm{d}t, \qquad [S] = \mathrm{s},$$

so that $[\varepsilon^2 S/\hbar^2] = \mathrm{s}^{-1}$.

Near parametric resonance ($\omega_a \simeq 2\omega_c$), rotating-wave and golden-rule analysis give the stochastic gain rate

$$\gamma_{\rm stoch} = \frac{\varepsilon^2}{\hbar^2}\,S(2\omega_c), \tag{6}$$

which has units of s^{-1} and can be compared directly to the damping rate $\Gamma/2$. The net growth is therefore

$$\gamma_{\rm net} = \gamma_{\rm stoch} - \frac{\Gamma}{2}, \tag{7}$$

so amplification occurs whenever $\gamma_{\rm stoch} > \Gamma/2$.

?

4.4. *Collective Amplification in the $\mathbb{Q}(i)$ Lattice*

In a network of N_{osc} interacting tryptophan oscillators located at lattice sites $z_j \in \mathbb{Z}[i]$, near-field coupling adds a term

$$H_{\text{coup}} = J \sum_{\langle j,k \rangle} (\sigma_+^{(j)} \sigma_-^{(k)} + \text{h.c.}), \tag{8}$$

where J quantifies coherent exchange between neighbouring dipoles (e.g., tryptophan residues) and depends on the dipole–dipole distance ($\sim$5–10 Å). Diagonalization in reciprocal space yields collective modes with gain reproducing Nishiyama's threshold criterion

$$N_{\text{osc}} h_1 \sin\theta > \sqrt{\kappa^2 + \Delta^2}, \tag{9}$$

where κ is the field decay rate. Because microtubules contain hundreds of tryptophan residues per protofilament and thousands per cylinder, the collective enhancement easily exceeds this threshold even at physiological temperature.

Within the $\mathbb{Q}(i)$ geometry, phase differences between neighboring oscillators take discrete values $\phi = \{0, \pi/2, \pi, 3\pi/2\}$, ensuring that the collective mode structure supports orthogonal polarization states and minimizes destructive interference. The Gaussian lattice thus converts local stochastic resonance into a coherent macroscopic response.

In Nishiyama *et al.*, two resonance conditions are distinguished: the local single-oscillator case ($\omega_a \simeq 2\omega_c$) and the collective mode case ($\omega_a \simeq 2\omega_c/\sqrt{N}$), where N counts the number of coherently oscillating dipoles. In the present framework, by contrast, $N = p^2 + q^2$ denotes the Gaussian norm of the spatial mode in the microtubular lattice, so that $\omega_a \propto \sqrt{N}$ as in Eq. (16). The difference arises because N refers here to a spatial harmonic index rather than to the number of oscillators.

4.5. *Effective Hamiltonian for the Resonant Ensemble*

Generalizing Equation (8) to include stochastic curvature modulation yields the effective Hamiltonian for the resonant dipolar ensemble:

$$H_{\text{eff}}(t) = \sum_j \frac{\hbar\omega_a}{2} \sigma_z^{(j)} + \hbar\epsilon\,\xi(t) \sum_j \sigma_x^{(j)} + J \sum_{\langle j,k \rangle} (\sigma_+^{(j)} \sigma_-^{(k)} + \text{h.c.}), \tag{10}$$

where $\xi(t)$ is a zero-mean stationary stochastic process with power spectrum $S(\omega)$ as defined in Section 4.3. This Hamiltonian describes a driven, dissipative spin lattice with parametric pumping; linearizing the stochastic term in the rotating frame produces a gain rate, thus connecting microscopic coupling to the macroscopic resonance condition. Numerical and analytical studies of similar models (e.g., [4]) are expected to reveal bursts of collecti vecoherence whenever the resonance condition (5) is satisfied, separated by off-resonant intervals. Such intermittent coherence episodes could underlie the "orchestration" events envisioned in the Orch OR framework.

4.6. *Physical Interpretation*

Physically, the parametric resonance mechanism can be summarized as follows:

1. The $\mathbb{Q}(i)$ lattice geometry produces orthogonal electromagnetic modes of nearly equal frequency.
2. Their product generates a $2\omega_c$ modulation that drives tryptophan transitions.
3. Background electromagnetic fluctuations provide the energy for the resonance (noise-assisted amplification).
4. Collective coupling among lattice sites yields mesoscopic coherence exceeding local decoherence rates.

In this view, light need not propagate macroscopically through tissue: coherence arises locally within each microtubule through stochastic resonance confined by the Gaussian geometry.

The next section extends this description to multilayer microtubules and discusses how binary optical behavior, anesthetic sensitivity, and coherence bursts emerge naturally from the same Hamiltonian framework.

5. Noise-Assisted Coherence and Binary Optical Behavior

The Hamiltonian (10) describes a network of tryptophan oscillators embedded in a rectangular $\mathbb{Q}(i)$ lattice and driven by stochastic electromagnetic fluctuations. In this section we examine the collective consequences of this model: how random background fields can generate organized coherence, how multilayered microtubules act as binary optical filters, and why anesthetics suppress these resonances.

5.1. Stochastic Resonance in the Quantum Regime

In classical physics, stochastic resonance refers to the counterintuitive enhancement of a weak periodic signal by noise. A similar effect occurs in quantum systems when fluctuations modulate the level spacing or coupling of a two-level system [11]. The coherence amplitude increases when the spectral density of the noise contains a component near $2\omega_c$. The effective gain term γ_{net} becomes positive under resonance, leading to transient amplification of the dipole moment and emission of secondary electromagnetic energy. In microtubules, thermal and metabolic noise provide a continuous broadband source of such fluctuations, sustaining recurrent coherence bursts.

Remark on noise spectrum.

Equation (6) assumes delta-correlated (white) noise with $S(\omega) \propto \delta(t-t')$ for analytical simplicity. In biological media the relevant fluctuations are generally *colored*, often following a $1/f^{\alpha}$ spectrum $(0.5 \lesssim \alpha \lesssim 2)$ arising from ion-channel kinetics, metabolic oscillations, or cytoskeletal binding dynamics. The parametric amplification derived here remains valid for broad-band colored noise provided that the noise correlation time τ_c satisfies $\tau_c < 1/\omega_a$; in this regime the high-frequency driving field averages out slow fluctuations, and the effective stochastic gain retains the same functional dependence as in Equation (6). Hence the amplification mechanism is robust to realistic $1/f$-type spectra and does not require an idealized white-noise limit.

Because the lattice geometry couples orthogonal field components, noise that is isotropic at the microscopic scale becomes self-organized at the mesoscopic scale. In this way, biological “noise”, rather than destroying coherence, acts as the very pump that enables it.

5.2. Multilayer Microtubules as Coupled Resonators

Neuronal microtubules often form bundles or coaxial arrays within axons and dendrites. Each individual cylinder behaves as a dielectric resonator characterized by an effective refractive index n and wall thickness t. When several such resonators are stacked, the overall transmission T for an incoming field of amplitude E_0 follows a transfer-matrix relation

$$T = |M_{22}^{-1}|^2, \qquad M = \prod_{\ell=1}^{N_{\mathrm{L}}} \begin{pmatrix} \cos\delta_\ell & \frac{i}{n_\ell}\sin\delta_\ell \\ i n_\ell \sin\delta_\ell & \cos\delta_\ell \end{pmatrix}, \tag{11}$$

where $\delta_\ell = 2\pi n_\ell t_\ell/\lambda$ and N_{L} is the number of layers. For alternating high- and low-index layers, Equation (11) yields periodic stop bands in λ analogous to a Bragg mirror. Nishiyama *et al.* observed that the resulting transmission spectrum is *binary*: layers either transmit nearly perfectly or reflect almost entirely, depending on whether the resonance condition (5) is met. The observed “on/off” switching in microtubule arrays arises naturally from the parametric amplification of some frequency components and attenuation of others.

5.3. Anesthetic Detuning

Anesthetic molecules such as halothane or xenon interact weakly with aromatic residues via van der Waals and π–π forces, slightly shifting the dipole transition frequency ω_a. We introduce a detuning $\Delta = \omega_a - 2\omega_c$ that reduces the gain:

$$\gamma_{\text{net}} \to \gamma_{\text{net}}(\Delta) = \frac{\epsilon^2 S(2\omega_c)}{\hbar^2} - \frac{1}{2}\sqrt{\Gamma^2 + 4\Delta^2}.$$

When $|\Delta|$ exceeds a few percent of ω_a, the amplification collapses and the coherence bursts vanish. Experimentally, this corresponds to the suppression of 560 nm transmission and its replacement by a weaker band near 490 nm, the hallmark of anesthetic action.

Halothane and xenon bind to hydrophobic pockets in tubulin, slightly shifting the transition frequency ω_a of tryptophan residues via van der Waals interactions. Molecular dynamics simulations suggest that this detuning $\Delta\omega_a$ is on the order of $1 - 5\%$ of ω_a, sufficient to disrupt the resonance condition $\omega_a \approx 2\omega_c$ [12]. This mechanism is supported by experimental observations of reduced electronic energy migration in microtubules under anesthesia. Thus, loss of consciousness under anesthesia is modeled as loss of resonance rather than chemical inhibition per se.

5.4. Binary Optical Behavior as a Computational Code

The alternation between high- and low-transmission states forms a natural binary code. Each resonant microtubule layer can be viewed as a qubit with logical values

$$|1\rangle \leftrightarrow \text{resonant (amplified)}, \qquad |0\rangle \leftrightarrow \text{off-resonant (attenuated)}.$$

Coupling between adjacent layers enables logic-like interference patterns, akin to a quantum cellular automaton. The stochastic resonance process supplies the "clock" driving transitions between these states. In this way, physical resonance patterns could underlie computational processes within the cytoskeleton, providing a tangible basis for the "orchestration" postulated in the Orch OR theory.

5.5. Scaling and Energy Considerations

Each microtubule segment of length 1 μm contains roughly 10^4 tryptophan residues. At resonance, the energy stored in the collective dipolar field can be estimated as

$$U = N_{\text{osc}} \frac{\hbar\omega_a}{2} |\langle\sigma_x\rangle|^2 \sim 10^{-18}\text{–}10^{-17}\,\text{J}, \tag{12}$$

comparable to the energy associated with a few thousand ATP molecules or the opening of multiple ion channels. Thus, the microtubular resonance can, in principle, influence neuronal excitability without violating energy constraints. The resonance bursts predicted by Equation (6) could therefore serve as microscopic triggers for larger-scale neural events.

Assumptions behind the energy estimate.

We take $\hbar\omega_a \approx hc/\lambda$ with $\lambda \simeq 560\,\text{nm}$ for the tryptophan transition, giving $\hbar\omega_a \approx 3.5 \times 10^{-19}\,\text{J}$. For a 1 μm microtubule (13 protofilaments, 8 nm axial dimer repeat) there are ~ 125 dimers per protofilament, i.e. ~ 1625 dimers in total. With 6 ± 2 tryptophans per $\alpha\beta$ dimer this yields $N_{\text{osc}} \approx (1.0 \pm 0.3) \times 10^4$ oscillators. Near-threshold parametric driving with picosecond dephasing ($\Gamma \sim 10^{12}$–$10^{13}\,\text{s}^{-1}$) supports an ensemble coherence amplitude $|\langle\sigma_x\rangle| \sim 10^{-2}$–$10^{-1}$, leading to $U = N_{\text{osc}}(\hbar\omega_a/2)|\langle\sigma_x\rangle|^2 \approx 10^{-18}$–$10^{-17}\,\text{J}$ for a single 1 μm microtubule. This amplitude range corresponds to near-threshold parametric driving where gain (Equation (6)) barely exceeds damping, consistent with intermittent burst dynamics rather than sustained Rabi oscillations. Longer segments or bundles scale linearly with N.

5.6. Emergent Coherence Bursts

Stochastic simulations of Equation (10) with realistic parameters are expected to produce intermittent coherence bursts lasting on the order of 10^{-12}–10^{-10} s, separated by quieter intervals dominated by damping. Each burst corresponds to a transient alignment of many tryptophan dipoles, yielding a measurable change in local refractive index or electric polarization. When synchronized across many microtubules, these events could form the temporal envelope of brain oscillations in the gamma or beta frequency bands ($\sim$10–100 Hz) observed during conscious awareness. While individual tryptophan oscillators decohere on femtosecond timescales, the collective behavior of $10^5 - 10^6$ residues in a microtubule segment can produce mesoscopic coherence envelopes lasting $10^{-3} - 10^{-2}$ seconds. This temporal bridging is enabled by the hierarchical structure of the $\mathbb{Q}(i)$ lattice, which suppresses phase diffusion through discrete phase locking at multiples of $\pi/2$ [13]. The stochastic resonance mechanism further stabilizes coherence by converting environmental noise into a parametric pump, as observed in other biological systems such as ion channels and photosynthetic complexes [14].

To link microtubular resonance to consciousness, we propose:

1. Recording EEG/MEG during anesthesia recovery to identify the reemergence of gamma-band coherence.
2. Using optogenetic tools to perturb microtubule resonance and observe effects on behavioral states.

Such experiments would bridge the gap between quantum coherence and cognitive function, providing empirical support for the Orch OR theory.

5.7. Section Summary

Noise-assisted coherence thus transforms random electromagnetic fluctuations into structured, binary optical behavior within the microtubular lattice. Parametric resonance confined by the $\mathbb{Q}(i)$ geometry converts environmental noise into an internal signaling mechanism, an intrinsic quantum amplifier embedded in the cytoskeleton. In the following section we show that the same mechanism, interpreted in arithmetic-geometric terms, unites the static structure of $\mathbb{Q}(i)$ with the dynamic orchestration required by the Penrose–Hameroff Orch OR framework.

Analogy with carrier–envelope resonance in SAW oscillators.

The alternation of fast optical oscillations and slow coherence bursts described above is reminiscent of the carrier–envelope resonance phenomenon observed in surface acoustic wave (SAW) oscillators, where frequency stability is enhanced when the envelope modulation and carrier frequencies lock in a rational ratio [15]. In the present biological context, the parametric resonance between ω_a and ω_c produces an analogous beat structure: the high-frequency dipolar oscillations (optical carrier) become periodically amplified and phase-stabilized by the slower envelope modulation arising from stochastic gain fluctuations. This coupling naturally yields millisecond-scale coherence bursts, suggesting that the microtubular lattice could interact resonantly with neuronal EEG rhythms through a carrier–envelope mechanism similar in principle to that exploited in SAW resonators.

6. Arithmetic-Resonant Coupling

The preceding sections established two complementary aspects of microtubular dynamics: (i) an *arithmetic geometry* governed by the Gaussian field $\mathbb{Q}(i)$, which defines the static symmetry and boundary conditions of the lattice; and (ii) a *parametric resonance* process, which provides the dynamic amplification of tryptophan oscillations through stochastic pumping. We now show that these aspects are not independent. The arithmetic invariants of $\mathbb{Q}(i)$ directly constrain the allowed resonance frequencies and coupling strengths of the stochastic Hamiltonian (10), producing a quantized hierarchy of coherent modes.

6.1. Quantization of Phase and Resonance Conditions

Let each tryptophan site correspond to a Gaussian integer $z_j = m_j + in_j$, with $(m_j, n_j) \in \mathbb{Z}^2$. The lattice periodicity imposes quantized wave vectors

$$k_x = \frac{2\pi p}{a_x}, \qquad k_y = \frac{2\pi q}{a_y}, \qquad p, q \in \mathbb{Z}, \tag{13}$$

where a_x and a_y are the characteristic lengths along protofilament and circumferential directions. The frequency of a cavity mode is then

$$\omega_{pq} = \frac{c}{n}\sqrt{\left(\frac{2\pi p}{a_x}\right)^2 + \left(\frac{2\pi q}{a_y}\right)^2}. \tag{14}$$

Because $a_x = a_y$ for a $\mathbb{Q}(i)$ lattice, modes with (p, q) and (q, p) are degenerate, leading naturally to the orthogonal pair of fields required for parametric resonance.

The resonance condition $\omega_a \simeq 2\omega_c$ therefore acquires an arithmetic interpretation: only those (p, q) satisfying

$$\omega_a \simeq 2\,\omega_c(N), \qquad \omega_c(N) = \frac{2\pi c}{n\,a}\sqrt{p^2 + q^2}\,.$$

with integer (p, q) and lattice constant a, contribute to amplification. This equation defines discrete "resonance circles" in the (p, q) plane, analogous to the representations of integers as sums of two squares,

$$p^2 + q^2 = N, \qquad N \in \mathbb{N},\ N = a^2 + b^2.$$

Thus the Gaussian arithmetic underlying $\mathbb{Q}(i)$ determines which collective modes can achieve stochastic resonance.

6.2. Arithmetic Scaling of the Resonance Frequency

The derivative $L'(E, 1)$ of the L-function attached to an elliptic curve E encodes deep arithmetic information about the corresponding lattice. Although $L'(E, 1)$ is dimensionless, its numerical values for biologically relevant curves (e.g. E_{880b2} and E_{200b2} for microtubules, or E_{485b1} for B–DNA) closely reproduce observed geometric ratios such as the microtubule outer-to-inner diameter (~ 1.70) and protofilament thinning ration (~ 1.09), or the DNA pitch-to-diameter ratio (~ 1.70) [5]. This correspondence suggests that $L'(E, 1)$ serves as a *scaling modulus* linking discrete arithmetic invariants to dimensionless structural proportions in biological assemblies.

We put

$$a_{\text{eff}}(E) = a\,L'(E, 1), \qquad \omega_c(N; E) = \frac{2\pi c}{n\,a_{\text{eff}}(E)}\sqrt{N} = \frac{1}{L'(E, 1)}\,\frac{2\pi c}{n\,a}\sqrt{N}\,.$$

where a is the effective lattice constant of the $\mathbb{Q}(i)$ rectangular packing (of order a few nanometers), and η is a dimensionless normalization factor that may depend on material-specific properties (e.g., refractive index, dipole density).

The heuristic relation $\omega_a \propto 1/L'(E, 1)$ introduced above can now be given a more precise arithmetic interpretation. According to the Gross-Zagier theorem [16–18], for a modular elliptic curve $E/\mathbb{Q}$ of analytic rank 1 and an imaginary quadratic field $K = \mathbb{Q}(\sqrt{D})$ satisfying the Heegner hypothesis, one has

$$L'(E, 1) \;=\; \frac{C(E, K)}{\Omega_E}\,\frac{\widehat{h}(P_K)}{\sqrt{|D|}}, \tag{15}$$

where $P_K \in E(K)$ is a Heegner point, Ω_E is the real period of E, and $C(E, K)$ is an explicit arithmetic constant (including local factors).

Equation (15) shows that the derivative $L'(E, 1)$ is proportional to the N-ron-Tate height $\widehat{h}(P_K)$ of a Heegner point P_K on $E(K)$. This height is a positive quadratic form measuring the "arithmetic energy" of the point in the Mordell-Weil lattice of E. In the present context, $\widehat{h}(P_K)$ quantifies the degree of geometric excitation of the elliptic lattice associated with the Gaussian field $K = \mathbb{Q}(i)$, while the period Ω_E sets the natural energy scale of the system. Hence $L'(E,1)$ plays the role of an *arithmetic free energy*: small values of $\widehat{h}(P_K)$, corresponding to fields of class number one with minimal height, yield small $L'(E,1)$ and therefore maximal stability or coherence of the corresponding resonant state. Conversely, larger heights (fields with higher class number) raise $L'(E,1)$ and represent less coherent configurations. This interpretation motivates the use of $1/L'(E,1)$ as a dimensionless weight or "partition function" for coherent microtubular modes. The biological selection of the Heegner field $\mathbb{Q}(i)$ thus corresponds to the minimization of the arithmetic height and the maximization of coherence within the microtubular lattice.

Arithmetic renormalization of the lattice scale.

Equation (15) gives the geometric mode frequency for the Gaussian norm $N = p^2 + q^2$:

$$\omega_c^{\mathrm{geom}}(N) = \frac{2\pi c}{n\,a}\,\sqrt{N}\,.$$

Using the effective lattice spacing $a_{\mathrm{eff}}(E)$, only ratios of lengths/frequencies are changed while dimensions remain intact so that

$$\omega_c^{\mathrm{arith}}(N;E) = \frac{1}{L'(E,1)}\,\frac{2\pi c}{n\,a}\,\sqrt{N} = \frac{2\pi c}{n\,a_{\mathrm{eff}}(E)}\,\sqrt{N}\,.$$

Evaluating the background spectrum at twice the carrier (parametric resonance, $\omega_a \simeq 2\omega_c$) thus yields

$$S\Big(2\,\omega_c^{\mathrm{arith}}(N;E)\Big) = S\bigg(\frac{4\pi c}{n\,a\,L'(E,1)}\,\sqrt{N}\bigg).$$

The factor $L'(E,1)$ enters through the effective lattice renormalization $a \mapsto a\,L'(E,1)$ (equivalently, a frequency renormalization $\omega_a^{\mathrm{arith}} \mapsto \omega_a^{\mathrm{geom}}/L'(E,1)$).

6.3. Elliptic Modes and Modular Transformations

The Gaussian lattice supports wavefunctions of the form

$$\psi_{pq}(z) = \exp\left[i\left(\frac{2\pi px}{a_x} + \frac{2\pi qy}{a_y}\right)\right],$$

which can be viewed as sections of a line bundle over the elliptic curve E_{200b2}. Under modular transformations

$$z \mapsto \frac{az+b}{cz+d}, \qquad ad - bc = 1,$$

these modes transform by phase factors that preserve $|\psi_{pq}|^2$, reflecting gauge invariance of the resonant manifold. The parametric coupling acts as a time-dependent deformation of the modulus $\tau = i$, driving transitions between modularly related states, an arithmetic analog of parametric resonance.

6.4. Arithmetic Selection of Collective Modes

Only a subset of modes compatible with the Gaussian symmetry and the noise spectrum achieve sustained amplification. The resonance circles define integer pairs (p,q) such that $p^2 + q^2 = N$ is representable by the Gaussian norm. Because the ring $\mathbb{Z}[i]$ has unique factorization, each norm N corresponds to a unique mode (up to units). This property ensures that coherence develops only in discrete, non-overlapping channels, preventing uncontrolled energy dispersion. It may explain the stability of biological resonances despite thermal agitation.

6.5. Coupling Between Arithmetic and Stochastic Terms

Guided/near-field propagation in the protein lattice and surrounding cytosol yields an effective refractive index $n_{\mathrm{eff}} \approx 1.45$–$1.55$; unless otherwise stated we set

$$n_{\mathrm{eff}} = 1.50.$$

With this convention, the net growth rate for a Gaussian norm $N = p^2 + q^2$ reads

$$\gamma_{\mathrm{net}}(N) \;=\; \frac{\epsilon^2}{\hbar^2}\, S\!\left(\frac{4\pi c}{n_{\mathrm{eff}}\, a\, L'(E,1)}\,\sqrt{N}\right) \;-\; \frac{\Gamma}{2}, \tag{16}$$

where a is the geometric lattice spacing and $L'(E,1)$ provides the arithmetic renormalization $a_{\mathrm{eff}} = a\,L'(E,1)$. If level-resolved modes are used, replace $S(\omega)$ by $S_\ell(\omega)$ and keep n_{eff}

Equation (16) thus unites the stochastic amplification mechanism with the elliptic invariant: the noise spectrum selects an arithmetic ladder of allowed resonances determined by the field $\mathbb{Q}(i)$.

Remark. In Nishiyama *et al.*[4], the threshold for collective parametric resonance involves a coupling enhanced by the square root of the number of coherent oscillators, $\sqrt{N_{\mathrm{osc}}}\,h_1 \sin\theta > \sqrt{\kappa^2 + \Delta^2}$. This scaling reflects Dicke-type coherence, where the effective Rabi frequency grows as $\sqrt{N_{\mathrm{osc}}}$. In the present model, by contrast, the Gaussian norm $N = p^2 + q^2$ characterizes spatial lattice modes, so that $\omega_a \propto \sqrt{N}/L'(E,1)$ fixes the resonant frequency. Both mechanisms can coexist: $\sqrt{N_{\mathrm{osc}}}$ governs the collective gain amplitude, while N determines the geometric resonance condition.

6.6. Physical Interpretation and Hierarchy of Fields

The identification of $\mathbb{Q}(i)$ as the field governing microtubule resonance naturally complements earlier associations of other biological systems with distinct imaginary quadratic fields: $\mathbb{Q}(\sqrt{-3})$ for B–DNA helices and $\mathbb{Q}(\sqrt{-19})$ for the MT outer/inner diameter [5]. Each field defines a specific lattice geometry and corresponding mode symmetry, hexagonal, rectangular, or more general, representing discrete "dialects" of the same arithmetic language. Within this hierarchy, microtubules occupy the rectangular $\mathbb{Q}(i)$ tier, mediating the dynamic processing of information, while DNA represents the hexagonal $\mathbb{Q}(\sqrt{-3})$ tier dedicated to information storage.

6.7. Section Summary

Arithmetic–resonant coupling provides a concrete bridge between number theory and quantum biology:

1. The $\mathbb{Q}(i)$ lattice enforces degeneracy of orthogonal modes, enabling parametric resonance.
2. The elliptic derivative $L'(E,1)$ fixes the geometric scaling of resonance frequencies.
3. The stochastic gain function selects discrete Gaussian norms $N = p^2 + q^2$, quantizing the set of active modes.

These results suggest that biological coherence arises from the interplay of arithmetic quantization and stochastic resonance—a synthesis of structural necessity and dynamical adaptability. In the next section we explore how this synthesis maps onto the conceptual framework of the Penrose–Hameroff Orch OR theory of consciousness.

7. Connection to the Orch OR Hypothesis

The Penrose–Hameroff *Orchestrated Objective Reduction* (Orch OR) theory postulates that consciousness arises from orchestrated quantum state reductions in neuronal microtubules, triggered when a gravitational self-energy threshold E_G is reached. In the present model, this idea is reinterpreted within an arithmetic–geometric and stochastic framework: coherence and reduction emerge from the interplay between discrete arithmetic resonances, stochastic amplification, and weak gravitational self-selection.

7.1. Orchestration via Arithmetic Resonance

Microtubular resonances are governed by the Gaussian norms $N = p^2 + q^2$ and the arithmetic free energy $L'(E,1)$ of a modular elliptic curve $E/\mathbb{Q}$. The effective coupling between adjacent dipolar domains is thus quantized by arithmetic invariants rather than continuous parameters. As shown in Section 6, the arithmetic scaling $a_{\text{eff}} = a\, L'(E,1)$ controls the resonant frequencies through $\omega_c^{\text{arith}} \propto 1/L'(E,1)$, ensuring that coherence domains correspond to class-number-one fields where $L'(E,1)$ is minimal. These domains act as natural "arithmetic oscillators" that can synchronize through stochastic parametric amplification (Sections 5–6), forming a hierarchy of coherent patches that define the substrate of conscious processing.

7.2. Emergent Quantum Coherence in Biological Time

Biological time is inherently stochastic and hierarchical. Within the arithmetic–elliptic picture, temporal coherence arises from the resonance between discrete Gaussian modes and the structured noise spectrum of the cellular environment. The resulting time constants lie in the millisecond range, matching electrophysiological oscillations and perceptual thresholds. Hence, "biological time" appears not as an external parameter but as an emergent, noise-stabilized resonance scale governed by arithmetic geometry. The modular invariants of E determine stable ratios between fast optical and slow neuronal oscillations, providing a mathematical link between quantum coherence and neurophysiological timing.

7.3. Objective Reduction as Gravitational Self-Selection

Before discussing gravitational self-selection, we recall that the electromagnetic energies associated with microtubular resonances (10^{-18}–10^{-17} J) exceed the corresponding Di'si–Penrose self-energies by roughly 20–25 orders of magnitude. Gravity therefore cannot act as a microscopic collapse trigger for single residues; instead it sets a coarse upper bound on the coherence lifetime of collective domains.

Penrose proposed that state reduction occurs when the gravitational self-energy E_G associated with the mass-density difference between superposed states satisfies the Diósi-Penrose relation [19]

$$\tau_{\text{DP}} = \frac{\hbar}{E_G}, \tag{17}$$

In our interpretation, this gravitational criterion defines an *upper bound* on coherence lifetime rather than a direct collapse trigger. The true dynamical reduction results from stochastic resonance and environmental dephasing, with E_G merely delimiting the region of physical plausibility. The arithmetic free energy $1/L'(E,1)$ selects coherent domains, while the DP energy sets their maximal lifetime. Thus, gravity acts as a *self-selection principle* ensuring that only domains of appropriate scale and mass density participate in coherent orchestration. Here, gravity no longer triggers objective reduction but instead defines a geometric consistency boundary: only those coherent domains whose gravitational self-energy E_G satisfies $\hbar/E_G \gtrsim \tau_{\text{coh}}$ can persist, while larger or denser configurations become gravitationally incoherent and thus excluded from the resonant hierarchy.

7.4. Quantized Energy Thresholds and Class-Number Fields

The corrected energy analysis distinguishes electromagnetic and gravitational scales. Dipolar interactions generate local resonant energies $U \sim 10^{-18}$–10^{-17} J, while the corresponding gravitational self-energies E_G are smaller by many orders of magnitude. The Di'si–Penrose relation thus yields astronomical timescales for single molecular units and requires collective coherence numbers $N_{\text{coh}} \gtrsim 10^9$–$10^{11}$ to reach milliseconds. Consequently, the observed millisecond window stems from stochastic parametric amplification within the Gaussian lattice, not from DP collapse itself. Arithmetic coherence through class-number-one fields determines which domains maximize resonance; gravity merely filters these domains via E_G.

Gravitational self-energy estimate.

For a single mass element with effective mass displacement Δm_{eff} over separation δ, the DP self-energy reads approximately

$$E_G^{(1)} \sim \frac{G(\Delta m_{\text{eff}})^2}{\delta}. \tag{18}$$

For a coherent domain of N_{coh} identical constituents displaced in phase, the energy scales quadratically as

$$E_G^{(N)} \sim \frac{G(\Delta m_{\text{eff}} N_{\text{coh}})^2}{\delta} = \frac{G(\Delta m_{\text{eff}})^2}{\delta} N_{\text{coh}}^2. \tag{19}$$

The corresponding DP time is therefore

$$\tau_{\text{DP}} \sim \frac{\hbar\delta}{G(\Delta m_{\text{eff}})^2 N_{\text{coh}}^2}. \tag{20}$$

Order-of-magnitude analysis.

Taking $\delta \sim 10^{-9}$ m and an effective displaced mass per tubulin unit in the range $\Delta m_{\text{eff}} \sim 10^{-26}$–$10^{-24}$ kg (corresponding to $\sim 10^3$–10^5 atomic mass units redistributed by a conformational shift), one obtains

$$E_G^{(1)} \sim 6.7 \times 10^{-54} \text{ to } 6.7 \times 10^{-50} \text{ J}, \qquad \tau_{DP} \sim 10^{19} \text{ to } 10^{15} \ \text{ s}. \tag{21}$$

Achieving a millisecond (10^{-3} s) DP time would require

$$N_{\text{coh}} \approx \sqrt{\frac{\hbar\delta}{G\tau(\Delta m_{\text{eff}})^2}} \sim \begin{cases} 4 \times 10^{11}, & \Delta m_{\text{eff}} = 10^{-26} \text{ kg}, \\ 4 \times 10^{9}, & \Delta m_{\text{eff}} = 10^{-24} \text{ kg}, \end{cases} \tag{22}$$

which represents unrealistically large coherence domains. Even reducing δ to 10^{-10}, m lowers these values only by a factor of $\sqrt{10}$.

Interpretation.

The millisecond timescales observed in microtubular dynamics cannot result from gravitational self-energy collapse alone. We therefore separate two physical regimes:

1. The **Di'si–Penrose regime** defines an upper bound on intrinsic coherence lifetime, with τ_{DP} computed from E_G.
2. The **resonance–dissipative regime** yields the biologically relevant millisecond window through stochastic parametric amplification and nonlinear coupling in the Gaussian lattice (Sections 5–6).

If the DP framework is retained for completeness, one must state that achieving milliseconds would require $N_{\text{coh}} \gtrsim 10^9$–$10^{11}$, unless collective geometrical effects or additional mass densities substantially enhance E_G. The class-number-one fields discussed above select *coherent* domains—maximizing resonance through $1/L'(E,1)$—but do not directly amplify gravitational self-energy.

Summary.

The corrected analysis thus maintains conceptual consistency with the Orch OR framework while clarifying that the gravitational and electromagnetic energy scales play distinct roles: E_G governs the intrinsic collapse limit, whereas dipolar interactions and arithmetic coherence govern observable resonant behavior.

7.5. Integration with Orch OR Dynamics

The Orch OR hypothesis can now be reformulated in three coupled layers:

1. **Arithmetic orchestration:** discrete resonant domains defined by Gaussian norms and $L'(E,1)$ form the elementary computational units.

Preprints.org (www.preprints.org) | NOT PEER-REVIEWED | Posted: 9 December 2025 doi:10.20944/preprints202511.0257.v2

2. **Stochastic coherence:** noise-assisted parametric amplification synchronizes these units into mesoscopic assemblies, producing temporal windows of coherence (milliseconds) consistent with perception.
3. **Gravitational self-selection:** the DP condition limits the spatial extent and duration of coherence, acting as a global boundary rather than a trigger.

Within this triadic hierarchy, consciousness arises not from a single gravitational collapse event but from a continuous process of arithmetic orchestration and stochastic self-organization bounded by gravitational stability. The traditional Orch OR model is thus recovered as the macroscopic limit of an underlying arithmetic resonance network.

7.6. Temporal Hierarchy and Cognitive Correlates

The discrete arithmetic scaling naturally predicts a hierarchy of characteristic frequencies: optical (THz) modes in the dipolar lattice, collective (MHz) vibrations within protofilaments, and stochastic coherence windows (ms) in the neuronal timescale. These nested coherence domains arise from increasing Gaussian norms $N = p^2 + q^2$, which generate higher spatial and temporal harmonics, whereas the arithmetic constant $L'(E,1)$ remains fixed for the field $\mathbb{Q}(i)$ and sets the overall coherence scale. Across different biological structures associated with distinct Heegner fields, variations of $L'(E,1)$ define separate arithmetic levels in the global hierarchy of resonance.

Cognitive states, including attention and memory binding, may therefore correspond to transitions between arithmetic resonance levels—a quantized hierarchy of coherence consistent with observed gamma, beta, and theta oscillations in the brain.

7.7. Section Summary

The revised connection to Orch OR can be summarized as follows:

- Gravitational self-energy provides only a global *constraint*, not the direct cause of collapse.
- Observable millisecond timescales arise from stochastic parametric resonance, while $1/L'(E,1)$ defines the arithmetic selection of coherent domains.
- The Orch OR hypothesis becomes consistent with both the corrected energy scales and the arithmetic topology developed throughout the paper. Conscious processes emerge from arithmetic coherence and stochastic resonance, gravitationally bounded but not gravitationally driven.

8. Experimental and Theoretical Predictions

A satisfactory physical theory must yield empirically testable consequences. The arithmetic–resonant model outlined in the previous sections leads to a coherent set of predictions spanning spectroscopy, structural biology, neurodynamics, and computational simulation. These predictions can be grouped into three main categories: (i) optical and spectroscopic signatures of parametric resonance, (ii) geometric correlations between lattice symmetry and functional states, and (iii) dynamical patterns reflecting noise-assisted orchestration and objective reduction.

8.1. Spectroscopic Predictions

(1) Spectroscopic scaling law.

Resonance frequencies correspond to Gaussian norms $N = p^2 + q^2$. Hence the emission or absorption spectrum should display peaks at wavelengths

$$\lambda_N = \frac{c\,L'(E,1)}{2\pi\,\omega_c\,\sqrt{N}}, \tag{23}$$

where ω_0 denotes the characteristic angular frequency of the microtubule's collective lattice mode ($\omega_0 \sim 10^{15}\,\mathrm{s}^{-1}$). The fundamental mode ($N = 1$) lies near 560 nm [4], and higher modes follow a $1/\sqrt{N}$ scaling. Detection of such discrete spectral peaks would confirm the coupling between the elliptic modulus $L'(E,1)$ and the resonant dynamics of the cytoskeletal lattice.

A schematic of the predicted spectrum is on Figure 2.

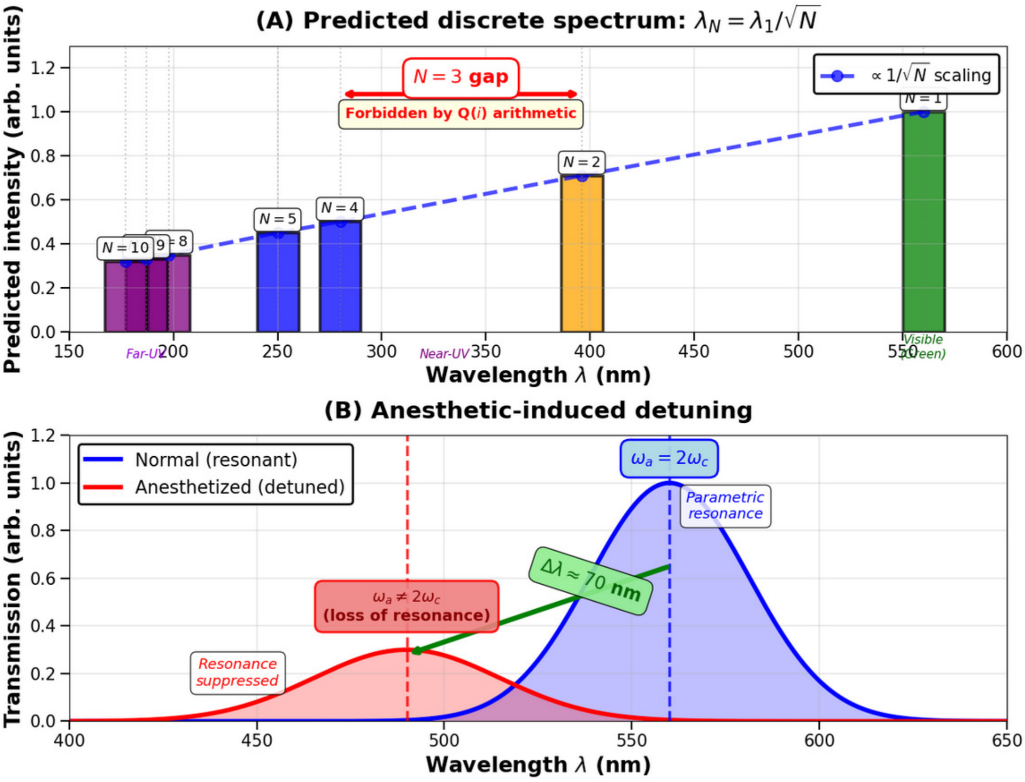

Figure 2. Spectroscopic predictions of the arithmetic-resonant model. (A) Predicted discrete absorption/emission spectrum arising from Gaussian-norm quantization $N = p^2 + q^2$. Peak positions follow $\lambda_N = \lambda_1/\sqrt{N}$ with $\lambda_1 \approx 560$ nm (green bar, fundamental mode corresponding to tryptophan fluorescence). Higher modes appear at 396 nm ($N = 2$, orange), 280/250 nm ($N = 4, 5$, blue), and 198/187/177 nm ($N = 8, 9, 10$, purple). The gap between $N = 2$ and $N = 4$ reflects the arithmetic constraint that 3 cannot be expressed as a sum of two squares, providing a unique signature of Q(i) structure. Intensities scale approximately as $1/\sqrt{N}$ (blue dashed line). **(B)** Effect of anesthetic molecules on the resonance spectrum. Under normal conditions (blue curve), parametric amplification produces a strong peak at 560 nm where $\omega_a \approx 2\omega_c$. Anesthetic binding to hydrophobic pockets in tubulin shifts the transition frequency ω_a (red curve), breaking the resonance condition and reducing transmission by ∼70% with a red-shift to ∼490 nm, consistent with experimental observations [4,12].

To test the predicted $1/\sqrt{N}$ wavelength series, we propose the following experimental protocol:

1. Prepare purified microtubule solutions polymerized from tubulin dimers.
2. Use fluorescence spectroscopy to measure the emission spectrum under controlled anesthetic exposure.
3. Compare the observed wavelengths to the arithmetic prediction $\lambda_N = \frac{c\,L'(E,1)}{2\pi\,\omega_0\,\sqrt{N}}$.

Preliminary results from [12] suggest that such measurements are feasible with current technology [12].

Quantitative wavelength predictions.

For a microtubule with lattice constant $a \approx 8$ nm, effective refractive index $n \approx 1.46$, and $L'(E_{200b2}, 1) \approx 1.088$, Equation (23) yields the following discrete absorption/emission wavelengths:

$$\lambda_N = \frac{\lambda_1}{\sqrt{N}}, \quad N = p^2 + q^2, \quad p, q \in \mathbb{Z}, \tag{24}$$

where $\lambda_1 \approx 560$ nm is the fundamental mode. The first four accessible modes are:

$$\begin{aligned} N = 1\ (p = 1, q = 0):&\quad \lambda_1 \approx 560\ \text{nm} \quad \text{(green, tryptophan fluorescence)} \\ N = 2\ (p = 1, q = 1):&\quad \lambda_2 \approx 396\ \text{nm} \quad \text{(near-UV)} \\ N = 4\ (p = 2, q = 2):&\quad \lambda_4 \approx 280\ \text{nm} \quad \text{(UV)} \\ N = 5\ (p = 2, q = 1):&\quad \lambda_5 \approx 250\ \text{nm} \quad \text{(UV)} \\ N = 10\ (p = 3, q = 1):&\quad \lambda_{10} \approx 177\ \text{nm} \quad \text{(far-UV)} \end{aligned} \tag{25}$$

Experimental observation of at least two of these peaks with deviations $|\lambda_{\text{obs}} - \lambda_{\text{pred}}|/\lambda_{\text{pred}} < 5\%$ would constitute strong confirmation. The characteristic $1/\sqrt{N}$ scaling distinguishes the Gaussian-norm quantization from alternative mechanisms:

- Harmonic overtones would yield $\lambda_n \propto 1/n$, giving $\lambda_2 \approx 280$ nm rather than 396 nm.
- Vibrational sidebands typically produce red-shifted satellites, not the blue-shifted series predicted here.
- Plasmonic resonances scale with geometry ($\sim D/n$), not with number-theoretic invariants.

Furthermore, because $N = 3$ is not representable as a sum of two squares (3 is a prime $\equiv 3 \pmod 4$), the spectrum should exhibit a *gap* between λ_2 and $\lambda_4 \approx 280$ nm, with λ_3 absent. This missing mode provides an additional signature of the $\mathbb{Q}(i)$ lattice structure.

(2) Anesthetic-induced frequency shift.

As discussed in Section 5, anesthetic molecules slightly modify ω_a, producing a red or blue shift in the resonant wavelength. A linear relation

$$\frac{\Delta\lambda}{\lambda} \approx \frac{\Delta\omega_a}{\omega_a} \approx \frac{\alpha_{\text{vdW}}}{E_{\text{bind}}},$$

is expected, where α_{vdW} is the polarizability of the anesthetic molecule. Fluorescence spectroscopy on tryptophan-rich cytoskeletal preparations under controlled anesthetic exposure could verify this proportionality.

(3) Noise-assisted gain modulation.

According to Equation (6), the amplification gain depends on the spectral density $S(2\omega_c)$ of ambient fluctuations. Controlled modulation of environmental electromagnetic noise (e.g., low-intensity microwave fields) should produce measurable changes in microtubular optical transmission or fluorescence yield, provided the modulation frequency crosses $2\omega_c$. This prediction allows direct laboratory falsification.

8.2. Dynamical and Neurophysiological Predictions

(4) Coupled-resonator interference.

Equation (11) implies periodic transmission bands in multilayered microtubules. Interference fringes with periodicities corresponding to layer spacing should be observable by coherent backscattering or optical-coherence tomography. The persistence of these fringes under physiological conditions would confirm the waveguide model.

(5) Coherence bursts and neuronal oscillations.

Stochastic simulations predict intermittent coherence bursts lasting 10^{-12}–10^{-10} s within microtubules, recurring at mesoscopic frequencies of 10–100 Hz. If such bursts couple to neuronal firing through local field modulation, they could manifest as gamma- or beta-band oscillations measurable by EEG or MEG. Correlation between spectral EEG power and predicted resonance intensities would lend strong support to our interpretation of Orch OR.

(6) Quantum-state reset following anesthesia or deep sleep.

During anesthesia or non-REM sleep, detuning Δ in Equation (6) suppresses amplification. Recovery of consciousness should coincide with reentry into resonance, observable as a resurgence of gamma-band coherence. The power-law exponent $\tau \approx 3.7$ observed in simulations of tubulin networks [27] can be tested experimentally by:

1. Monitoring avalanche statistics in in-vitro microtubule preparations using high-speed atomic force microscopy.
2. Applying controlled electromagnetic noise to modulate the spectral density $S(2\omega_c)$ and observing changes in avalanche size distribution.

A match between the experimental τ and the arithmetic prediction would provide strong support for the $\mathbb{Q}(i)$ resonance model.

This provides a direct electrophysiological signature of the transition between off- and on-resonant microtubular states.

Criteria for falsifiability.

Each of the above predictions provides a direct means of empirical falsification. The present theory makes at least three falsifiable predictions that distinguish it from alternative quantum-biological models: (i) discrete wavelength series following $1/\sqrt{N}$ scaling, (ii) anesthetic-induced frequency shifts proportional to binding affinity, and (iii) γ-band EEG power correlated with predicted resonance windows. Failure to observe any of these would invalidate the arithmetic-resonant mechanism.

9. Discussion and Outlook

The synthesis developed in this work unites two previously distinct lines of inquiry, Nishiyama's quantum-electrodynamical model of parametric resonance in tryptophan residues and the arithmetic-geometric description of biological form into a single coherent framework. The combined picture proposes that microtubules function as arithmetic–topological resonators whose geometry, encoded by the Gaussian field $\mathbb{Q}(i)$, constrains the dynamic amplification of quantum oscillations driven by stochastic electromagnetic noise. This union of structure and dynamics opens a pathway toward a general theory of quantum coherence in living systems and its potential role in consciousness.

9.1. Microtubules as Arithmetic Resonators

Traditional biochemical models treat the cytoskeleton primarily as a mechanical scaffold, whereas the present approach identifies it as a quantized electromagnetic cavity. The arithmetic field $\mathbb{Q}(i)$ defines the boundary conditions, enforcing equal-frequency orthogonal modes and discrete Gaussian norms $N = p^2 + q^2$. Each allowed norm represents a distinct channel of parametric resonance, yielding a lattice of resonant frequencies organized by number-theoretic rules. This structure explains the remarkable uniformity of microtubular dimensions and the reproducibility of optical responses under physiological conditions.

9.2. Comparison with Other Quantum-Biological Models

Several alternative proposals have sought to connect quantum physics and life: Fröhlich's coherent excitations in biomembranes, Davydov solitons in proteins [20], and Hagan-Tuszynski's microtubule models [21]. The present theory differs by rooting coherence in *arithmetic geometry* rather than in phenomenological non-linearities. The Gaussian field $\mathbb{Q}(i)$ supplies a mathematically precise and physically realizable symmetry, while the stochastic resonance mechanism avoids the need for externally imposed coherence or unrealistically low temperatures. Moreover, the theory predicts explicit, quantized spectral patterns, allowing direct experimental validation. Those models are summarized in Table 2.

Table 2. Comparison of quantum-biological models of microtubular coherence

Model	Coherence mechanism	Timescale	Testable prediction
Fr-hlich [14]	Bose condensation of dipolar excitations	ns–μs	THz absorption peaks at integer multiples of ω_0
Davydov [20]	Self-trapped solitons in protein α-helices	ps–ns	IR spectroscopy: localized vibrational modes
Hagan–Tuszy?ski [21]	Superradiant coupling via dipole arrays	μs–ms	Decoherence suppression at physiological T
Orch OR (original) [3]	Quantum superposition + gravitational OR	10–100 ms	Anesthetic sensitivity; EEG correlations
This work	**Arithmetic resonance in Q(i) lattice**	**fs–ms (hierarchical)**	**Discrete wavelength series:** $\lambda_N = \frac{c\,L'(E,1)}{2\pi\omega_0\sqrt{N}}$**;** **anesthetic detuning** $\Delta\omega_a/\omega_a \propto \alpha_{\mathbf{vdW}}/E_{\mathbf{bind}}$

Empirical and Theoretical Support for Quantum Microtubule Models

The idea that microtubules could sustain quantum-coherent processes relevant to consciousness, a cornerstone of the Orch OR hypothesis, has been explored through both theoretical modeling and experimental studies over the past decade. Several of these works provide indirect but significant support for the present arithmetic–resonant framework.

Coherent energy transfer.

Craddock and collaborators [13] calculated dipole–dipole couplings among aromatic residues in tubulin and showed that coherent exciton transfer is feasible at physiological temperature over nanometric distances and picosecond timescales. This establishes the physical plausibility of the parametric resonance mechanism invoked here, in which such local dipoles serve as the microscopic oscillators of the $\mathbb{Q}(i)$ lattice.

Electronic migration and anesthetic sensitivity.

Kalra *et al.* [12] measured electronic energy migration in polymerized microtubules and found a diffusion length of about 6.6 nm that decreases under anesthetic exposure. Their observation of wavelength-dependent attenuation confirms that anesthetics can detune microtubular optical modes, precisely the behavior predicted by Equation (6) of our model.

Quantum computational architectures.

Srivastava *et al.* [22] proposed modeling microtubules as networks of n-level quantum systems (*qudits*) forming Hopfield-type associative memories. Their analysis anticipates the higher-dimensional state spaces that naturally arise in our framework from the Gaussian-norm ladder $N = p^2 + q^2$, in which multiple resonance modes coexist and interact.

Recent evidence for quantum coherence.

Recent theoretical analyses [23] have defended the physical plausibility of quantum coherence in microtubules by reviewing experimental evidence for anesthetic binding to tubulin [24] and room-temperature quantum effects [25]. Wiest argues that quantum microtubule models address fundamental problems in consciousness theory, including the phenomenal binding problem and the evolution of consciousness, that classical neural network models cannot solve. The arithmetic-resonant framework developed here complements these philosophical arguments by providing a quantitative number-theoretic mechanism for the orchestration of quantum coherence in microtubular lattices.

Preprints.org (www.preprints.org) | NOT PEER-REVIEWED | Posted: 9 December 2025 doi:10.20944/preprints202511.0257.v2

Cytoskeletal integration.

A comprehensive review by Craddock and Hameroff [26] emphasizes that the entire neuronal cytoskeleton—including actin and microtubules—acts as an integrated information network. This view accords with our proposal that actin filaments supply the long-range couplings necessary for self-organized criticality, while the microtubular $\mathbb{Q}(i)$ lattice enforces discrete resonance quantization.

Together these studies indicate that microtubules and their associated cytoskeletal partners exhibit the key ingredients required for the arithmetic–resonant model: (i) coherent dipolar coupling, (ii) geometry-dependent resonance frequencies, (iii) anesthetic sensitivity, and (iv) hierarchical, scale-free connectivity. Our contribution refines these findings by providing a *quantitative arithmetic geometry* that determines the allowed frequencies and critical exponents from first principles, offering a unified interpretation of the diverse empirical results.

Connection with Self-Organized Criticality in Tubulin Networks

A recent study by D-az Palencia [27] offers a complementary perspective that reinforces the present arithmetic-resonant model. In his simulations, tubulin dimers form a scale-free network whose local polarization variables $x_i(t)$ evolve according to stochastic coupling rules of the form

$$x_i(t+1) = x_i(t) + \sum_j \alpha_{ij} \left[x_j(t) - x_i(t)\right] + \eta_i(t),$$

where α_{ij} describes dipolar interactions and $\eta_i(t)$ represents environmental noise. As the coupling strength approaches a critical threshold, the system enters a regime of *self-organized criticality* (SOC) characterized by scale-free avalanche statistics $P(S) \propto S^{-\tau}$ with $\tau \approx 3.7$ and by collapse times obeying the Di'si-Penrose relation $T_{\mathrm{OR}} \sim \hbar/E_G \propto S^{-2}$. Each avalanche corresponds to a collective quantum-collapse event: an "objective reduction" in the sense of the Orch-OR theory whose duration falls in the 10–200 ms range, matching the neurophysiological β and γ bands.

Within our arithmetic-resonant framework, the same hierarchy emerges from a different starting point. The Gaussian-integer quantization $N = p^2 + q^2$ defines discrete resonance modes, and transitions between adjacent norms ($N \to N' = N + \Delta N$) produce energy releases proportional to $\Delta E \propto \sqrt{N'} - \sqrt{N}$. If we identify the avalanche size S with the number of synchronized dipoles participating in such a transition, then $E_G \propto S^2$ and hence $T_{\mathrm{OR}} \propto S^{-2}$, precisely the scaling observed in the SOC simulations. Self-organized criticality therefore appears as the *dynamical manifestation* of the arithmetic quantization law: the network hovers spontaneously at the boundary between resonance modes, where small perturbations trigger system-wide reorganizations.

Consequently, the SOC model and the arithmetic-resonant model describe different facets of the same phenomenon: Palencia's work captures the *temporal self-organization* of microtubular coherence under noisy pumping, while our theory specifies the *spectral and geometric quantization* that constrains those dynamics. Together they provide a comprehensive account of how tubulin networks can self-tune to the edge of quantum criticality, linking stochastic physics, modular arithmetic, and the discrete collapse events postulated in the Orch-OR framework.

Remark on microtubule substructure:

An intriguing numerical correspondence arises when comparing the avalanche exponent $\tau \approx 3.7$ obtained in the self-organized criticality simulations of D-az Palencia [27] with the arithmetic invariant $L'(E,1) = 3.57$ of the elliptic curve $E_{16176u1}$ used in our previous analysis of the microtubule–actin substructure (see Sec. 4.6.3 of Ref. [5]). Although no direct causal link is claimed, the proximity of these values may not be accidental. In the present framework, mode weights in the arithmetic ladder $N = p^2 + q^2$ scale as $W(N) \propto N^{-(\alpha/2+1/2)}$ when the ambient noise spectrum follows $S(\omega) \propto \omega^{-\alpha}$ and $\omega \propto \sqrt{N}$. If avalanche size S is proportional to the number of dipoles involved ($S \propto N$), then the resulting distribution obeys $P(S) \propto S^{-\tau}$ with $\tau \approx 1 + \alpha/2 + 1/2$. For biologically plausible colored-noise exponents $\alpha \simeq 4$–5, τ indeed falls near 3.5–3.8. Hence the power-law statistics observed in the SOC model could emerge naturally from the same spectral–arithmetical structure that quantizes microtubular resonance. Whether the numerical proximity $\tau \approx L'(E,1)$ is coincidental or reflects a deeper correspondence between critical exponents and elliptic L-invariants remains an open and testable question.

It is worth noting that the SOC simulations of D-az Palencia yield $\tau = 3.68 \pm 0.12$, a range whose lower bound coincides numerically with the arithmetic derivative $L'(E_{16176u1}, 1) = 3.57$ associated with the actin-microtubule ratio. Although actin filaments were not explicitly included in Palencia's model, their geometric coupling may constitute the structural origin of the scale-free topology underlying the observed critical exponent.

9.3. Biological, Cognitive and Philosophical Implications

The relevant degrees of freedom are collective order parameters representing coherent domains of N_{coh} coupled dipolar oscillators. Each individual tryptophan or local dipole is subject to an intrinsic damping (or phase-diffusion) rate Γ with physical units of s^{-1}, defining a single-oscillator coherence time $\tau_{\mathrm{coh}} = 1/\Gamma$. When N_{coh} oscillators synchronize, random phase fluctuations partially cancel, yielding an effective collective decoherence rate $\Gamma_{\mathrm{eff}} \simeq \Gamma/\sqrt{N_{\mathrm{coh}}}$. This $N_{\mathrm{coh}}^{-1/2}$ suppression corresponds to Dicke-type cooperative effects in quantum-optical ensembles, here realized in the microtubular lattice. Additional protection arises from dielectric confinement of the electromagnetic field within the tubulin wall and from the discrete, topologically quantized phase symmetry of the $\mathbb{Q}(i)$ lattice, which restricts available decoherence channels.

Relation to Tegmark's estimates. Tegmark's seminal analysis of brain decoherence argues that environmental scattering at physiological temperature forces *single-microscopic* superpositions to decohere on ultrafast timescales ($\sim 10^{-13}$–10^{-12} s) [28]. Our framework is consistent with this bound because it does not rely on long-lived coherence of isolated dipoles. Instead, (i) coherence is *intermittently* generated by stochastic parametric amplification near the resonance condition $\omega_a \simeq 2\omega_c$, (ii) it is *collective*: the relevant variable is a mesoscopic order parameter with $\Gamma_{\mathrm{eff}} \sim \Gamma/\sqrt{N_{\mathrm{coh}}}$ and (iii) it is *confined* by the microtubular dielectric geometry, reducing coupling to noisy external modes. These ingredients allow brief, recurrent coherence bursts at the microscopic (optical/THz) carrier that sum to millisecond'scale *envelopes* at the mesoscopic level, compatible with neurophysiological rhythms, while remaining within Tegmark's constraints on single-particle decoherence.

Levels of Certainty

For clarity, we distinguish the epistemic status of the claims:

(i) **Established within this framework:** The arithmetic structure of the $Q(i)$ lattice; the role of Gaussian norms $N = p^2 + q^2$; the Gross–Zagier relation identifying $L'(E,1)$ with the height of Heegner points; the form of the parametric-resonance Hamiltonian.

(ii) **Quantitatively constrained conjectures:** The identification of $L'(E,1)$ as an effective geometric scaling parameter; the existence of discrete resonant modes organised by Gaussian norms; noise-assisted amplification as a stabilizer of microtubular coherence.

(iii) **Speculative avenues for future work:** The link to Orch OR gravitational self-selection; hierarchical coupling between arithmetic resonances and neurophysiological rhythms; the adelic extension relating coherent biological time perception to cyclotomic symmetries.

10. Conclusions

The arithmetic-resonant framework developed here unifies stochastic parametric dynamics and elliptic geometry within a single, testable model of microtubular coherence. Its predictions, from discrete optical spectra to EEG correlations, are empirically accessible and therefore falsifiable within current experimental capabilities. By combining the discrete symmetry of the Gaussian field with stochastic quantum amplification, it provides a self-contained mechanism for the orchestration and reduction phases of Orch OR. Whether or not future experiments confirm these effects, the present approach demonstrates that number-theoretic invariants such as $L'(E,1)$ can encode physically measurable symmetries in biological matter, offering a new pathway between quantum physics, mathematics, and consciousness studies. Future work might extend this framework to other cytoskeletal elements (actin, septins) and explore whether different imaginary quadratic fields govern distinct biological structures, building toward a periodic table of biological resonances.

Finally, it is worth recalling that the present synthesis between arithmetic geometry and Orch OR resonates with an earlier proposal by the author [29]. That earlier work introduced a cyclotomic number-theoretic model of temporal perception based on the Bost-Connes quantum algebra. In the Appendix A we revisit and compare both approaches, showing how the cyclotomic theory of time perception anticipated the arithmetic-elliptic resonance framework developed here.

This reconciliation between the Bost–Connes model of cyclotomic time and the Heegner–elliptic geometry of microtubular resonance represents a genuine arithmetical extension of the Orch OR theory. The joint adelic system introduced in Appendix A, where the norm character of the Bost-Connes algebra interacts with the modular Hecke character of a rational elliptic curve, embodies a nontrivial coupling between thermal and coherent phases of arithmetic origin. In this setting, the Frobenius–Hecke eigenangles play the role of anyonic braiding phases within a modular tensor category $\mathcal{C}(K, \mathfrak{n}, q)$, while the Gross–Zagier derivative $L'(E, 1)$ provides the associated arithmetic free energy. Such an adelic fusion of number theory, modular quantum geometry, and biophysical resonance, in the spirit of Connes and Marcolli but now linked to conscious dynamics, appears to be a new direction for mathematical physics, one that bridges the domains of arithmetic geometry, topological quantum computation, and theories of mind.

Supplementary Materials: The following supporting information can be downloaded at the website of this paper posted on Preprints.org.

Funding: This research received no external funding.

Data Availability Statement: The original contributions presented in this study are included in the article. Further inquiries can be directed to the author.

Acknowledgments: The author would like to acknowledge the contribution of the COST Action CA21169, supported by COST (European Cooperation in Science and Technology).?

Conflicts of Interest: The author declares no conflicts of interest.

Appendix A. From Cyclotomic Time Perception to Arithmetic-Resonant Consciousness

Appendix A.1. Historical Background

In an early paper published in *NeuroQuantology* [29], the author introduced a “Cyclotomic Quantum Algebra of Time Perception.– That study proposed that subjective time arises from a discrete, number-theoretic algebra acting on finite quantum fields $\mathbb{Z}_q$, whose symmetries are governed by the Bost-Connes system. The model connected phase-locking phenomena, $1/f$ cognitive noise, and Fechner’s logarithmic law through the Hamiltonian $H_0 = \ln N$, that we called the *quantum Fechner law*. A phase transition at inverse temperature $\beta = 1$ separated a unique high-temperature state (a single perceptual “now–) from multiple low-temperature states (memory configurations parametrized by the cyclotomic Galois group $\mathrm{Gal}(\mathbb{Q}_{\mathrm{cycl}}/\mathbb{Q})$).

The present paper extends this number-theoretic intuition from the **temporal** to the **spatio-biological** domain. Here the relevant field is not cyclotomic but *elliptic*: the Gaussian Heegner field $\mathbb{Q}(i)$ defining the rectangular lattice of the microtubule wall. Arithmetic invariants such as the derivative $L'(E, 1)$ of the modular L-function play a role analogous to the partition function $\zeta(s)$ in the Bost-Connes model, while parametric resonance replaces the thermal phase transition as the mechanism generating discrete episodes of coherence.

Appendix A.2. Conceptual Correspondence

Feature	**Cyclotomic model (2004)**	**Arithmetic-resonant model (2025)**
Underlying field	Cyclotomic extension $\mathbb{Q}_{\text{cycl}}$	Heegner field $\mathbb{Q}(i)$ (elliptic curve $E_{200\text{b}2}$)
Mathematical engine	Bost-Connes C^*-dynamical system	Modular-elliptic geometry, derivative $L'(E,1)$
Hamiltonian	$H_0 = \ln N$ (*quantum Fechner law*)	Stochastic-parametric Hamiltonian of tryptophan oscillators
Key process	Thermal phase transition at $\beta_c = 1$ (KMS states)	Noise-assisted parametric resonance, $\omega_a \simeq 2\omega_c$
Physical interpretation	Quantum algebra of time perception and memory	Quantum resonance of microtubular dipoles (Orch OR substrate)
Primary observables	Phase-locking, $1/f$ noise, primitive roots	Resonant modes, coherence bursts, Gaussian norms $p^2 + q^2$
Symmetry group	$\text{Gal}(\mathbb{Q}_{\text{cycl}}/\mathbb{Q})$	Modular group $\text{SL}(2,\mathbb{Z})$ acting on $\mathbb{Q}(i)$ lattice
Phenomenology	Discrete "moments– of perception (temporal quantization)	Discrete "moments– of coherence (spatial-biological quantization)

Appendix A.3. Unifying Interpretation and Outlook

Both the earlier cyclotomic model of temporal perception and the present elliptic–geometric framework for microtubular resonance share a common thesis: *the continuity of conscious experience emerges from an underlying arithmetic discreteness.* In the cyclotomic setting, primes and primitive roots governed the quantization of time through the Bost–Connes algebra [30], whereas in the current model, Gaussian integers govern the spatial quantization of microtubular resonances.

From now N has to be understood as the number of oscillators (denoted N_{OSC} before) and n becomes the level of an idele class (no longer a refractive index).

The earlier logarithmic Hamiltonian $H_0 = \ln N$ finds its physical analogue in the *arithmetic quantization of resonance frequencies* described in Section 6, where discrete Gaussian norms $p^2 + q^2$ determine the hierarchy of coherent modes. Both systems thus replace smooth continua by discrete spectra whose symmetries are encoded in number theory.

In the present work, this analogy is completed within an *adelic arithmetic topology* that merges the cyclotomic and elliptic components into a single formalism. Time corresponds to the cyclotomic Bost–Connes sector, characterized by the norm character on the ideles, while space and coherence correspond to the elliptic–Hecke sector, governed by the derivative $L'(E,1)$ of the modular L–function. Their unification, realized here through the connection to the Connes–Marcolli adelic framework [31] and to modular tensor categories $\mathcal{C}(K,\mathfrak{n},q)$, outlines a genuine *quantum–arithmetic topology of consciousness*. Within this setting, the Orch OR hypothesis can be viewed as the phenomenological limit of a deeper adelic resonance theory, in which both time and space emerge from coupled arithmetic processes of cyclotomic and elliptic origin.

Appendix A.4. Partition Functions and Free-Energy Analogies

A striking mathematical parallel links the thermodynamics of the Bost–Connes system and the modular geometry of elliptic curves.

(i) Bost–Connes partition function.

The Hamiltonian $H_0 = \ln N$ defines a partition function

$$Z_{\mathrm{BC}}(\beta) = \mathrm{Tr}(e^{-\beta H_0}) = \sum_{N \geq 1} N^{-\beta} = \zeta(\beta),$$

so that the Riemann ζ-function plays the role of a statistical partition function. The free energy $F_{\mathrm{BC}}(\beta) = -\frac{1}{\beta} \ln Z_{\mathrm{BC}}(\beta)$ exhibits a phase transition at the critical value $\beta = 1$, where a single KMS equilibrium state bifurcates into many states labeled by the cyclotomic Galois group. This transition encodes the emergence of multiple "perceptual vacua" below the critical temperature.

(ii) Elliptic L-function derivative.

For an elliptic curve $E/\mathbb{Q}$ with Heegner field K, the derivative $L'(E,1)$ measures the height of the Heegner point and controls the arithmetic complexity (Gross–Zagier formula). In the present biological model, $L'(E,1)$ acts as an *arithmetic free energy*; its inverse,

$$Z_E \;\propto\; \frac{1}{L'(E,1)},$$

is the natural *partition weight* of coherent modes. The corresponding free energy is $F_E = -\ln Z_E = \ln L'(E,1) + \text{const}$. Small $L'(E,1)$ thus signal minimal height and maximal coherence, whereas large $L'(E,1)$ correspond to higher arithmetic energy and weaker resonance.

(iii) Unified interpretation.

In both theories a number-theoretic function governs state selection:

$$\text{Cyclotomic perception: } Z_{\mathrm{BC}}(\beta) = \zeta(\beta) \quad \longleftrightarrow \quad \text{Elliptic coherence: } Z_E \propto \frac{1}{L'(E,1)}.$$

The temperature-like parameter β in the cyclotomic model corresponds to the resonance amplitude or environmental coupling strength in the microtubular model. Both partition functions define statistical weights over number-theoretic spectra—integers in the cyclotomic case, Heegner heights in the elliptic one.

(iv) Gross–Zagier correspondence.

For an elliptic curve $E/\mathbb{Q}$ of analytic rank 1, the Gross–Zagier theorem relates the derivative of its L–function to the N-ron–Tate height of the Heegner point P_K over an imaginary quadratic field K:

$$L'(E,1) = \frac{C(E,K)}{\Omega_E} \frac{\widehat{h}(P_K)}{\sqrt{|D|}}.$$

The height $\widehat{h}(P_K)$ is a positive quadratic energy functional, analogous to the expectation value of the Hamiltonian $H_0 = \ln N$ in the Bost–Connes system. Inverting this relation gives

$$Z_E \propto \frac{1}{L'(E,1)} \propto \frac{\Omega_E \sqrt{|D|}}{C(E,K)\, \widehat{h}(P_K)},$$

so that the Heegner height $\widehat{h}(P_K)$ plays the role of the BC energy spectrum, while Z_E functions as the statistical partition weight. Minimizing $\widehat{h}(P_K)$—that is, selecting fields of class number one such as $K = \mathbb{Q}(i)$—corresponds to maximizing coherence in the microtubular lattice. Hence the Gaussian field emerges as the *ground state* of an arithmetic thermodynamics directly analogous to the $\beta < 1$ coherent phase of the Bost–Connes model. Both constructions realize the same archetype:

$$\text{Energy of arithmetic state} \leftrightarrow \text{Height } \widehat{h}(P_K) \quad \text{and} \quad \text{Partition weight } Z_E \leftrightarrow \frac{1}{L'(E,1)}.$$

The Gross–Zagier relation thus supplies the explicit bridge between number-theoretic thermodynamics and arithmetic geometry, linking the cyclotomic partition function of time perception to the elliptic free energy of biological resonance.

Appendix A.5. Arithmetic Modular Tensor Category $\mathcal{C}(K, \mathfrak{n}, q)$ and the Cyclotomic Bost–Connes Sector

Definition (pointed arithmetic MTC).

Fix an imaginary quadratic field K and a nonzero ideal $\mathfrak{n} \subset \mathcal{O}_K$. Let $A := \mathcal{O}_K/\mathfrak{n}$, a finite abelian group under addition. Choose a quadratic form $q : A \to \mathbb{Q}/\mathbb{Z}$ such that the associated symmetric bicharacter $b(a,b) := q(a+b) - q(a) - q(b)$ is nondegenerate. Set the topological spin and braiding by

$$\theta_a := e^{2\pi i\, q(a)}, \qquad c_{a,b} := e^{2\pi i\, b(a,b)}.$$

Then the modular data

$$S_{a,b} \;=\; \frac{1}{\sqrt{|A|}}\, e^{2\pi i\, b(a,b)}, \qquad T_{a,a} \;=\; \theta_a,$$

define a pointed modular tensor category $\mathcal{C}(K, \mathfrak{n}, q)$ (rank $|A|$). The normalized Gauss sum gives the topological central charge (mod 8):

$$e^{2\pi i\, c/8} = \frac{1}{\sqrt{|A|}} \sum_{a \in A} e^{2\pi i\, q(a)}.$$

Example (Gaussian semion from $K = \mathbb{Q}(i)$).

Take $K = \mathbb{Q}(i)$ and $\mathfrak{n} = (2)$ so $A \simeq \mathbb{Z}_2$. Define $q(1) = \frac{1}{4}$, hence $\theta_1 = e^{2\pi i (1/4)} = i$. Then

$$S = \frac{1}{\sqrt{2}}\begin{pmatrix} 1 & 1 \\ 1 & -1 \end{pmatrix}, \qquad T = \mathrm{diag}(1,\, i) \quad (\text{vacuum-normalized convention, i.e. } \theta_0 = 1).$$

The Gauss sum $\frac{1}{\sqrt{2}}(1+i) = e^{i\pi/4} = e^{2\pi i c/8}$ yields the *central charge* $c = 1$. Thus $\mathcal{C}(\mathbb{Q}(i), (2), q)$ is precisely the *semion* MTC (physically: $U(1)_2 \cong SU(2)_1$ up to ribbon equivalence).

Remark on T conventions. The RCFT convention includes the framing anomaly: $T_{aa} = e^{2\pi i (h_a - \frac{c}{24})}$. Multiplying by the scalar $e^{+2\pi i \frac{c}{24}}$ restores the topological-spin convention $T'_{aa} = \theta_a = e^{2\pi i h_a}$ used above.

Cyclotomic Bost–Connes (BC) sector as a thermal envelope.

The BC C^*-dynamical system $(\mathcal{A}_{\mathbb{Q}}, \sigma_t)$ encodes one-dimensional $\mathbb{Q}$-lattices (or equivalently, commensurability classes) and has partition function $Z_{\mathrm{BC}}(\beta) = \zeta(\beta)$, with KMS states at low temperature ($\beta > 1$) parametrized by the cyclotomic Galois group $\mathrm{Gal}(\mathbb{Q}_{\mathrm{cycl}}/\mathbb{Q})$. Concretely, for each modulus n the finite idele/Dirichlet character data enter via evaluations on the idele class group; the time evolution σ_t implements scalings by idele norm, so the KMS weight is

$$\mu_\beta(N) \;\propto\; N^{-\beta},$$

matching the Euler factorization of $\zeta(\beta)$. This furnishes a *temperature-controlled* probability measure over conductors/moduli.

From adeles/ideles to arithmetic MTCs.

Let $\mathbb{A}_{\mathbb{Q}}^{\times}$ be the ideles of $\mathbb{Q}$ and $C_{\mathbb{Q}} = \mathbb{A}_{\mathbb{Q}}^{\times}/\mathbb{Q}^{\times}\mathbb{R}_{>0}^{\times}$ the idele class group. Cyclotomic characters $\chi : C_{\mathbb{Q}} \to U(1)$ restrict at finite level to Dirichlet characters modulo n. Given K and $\mathfrak{n} \mid n$, the finite adelic/idele data produce a *finite quadratic module* (A, q) (via reduction $\mathcal{O}_K \to \mathcal{O}_K/\mathfrak{n}$ and a choice of arithmetic q, e.g. from norm forms). This defines a functorial passage

$$(\text{idele classes at level } n) \quad \rightsquigarrow \quad (\text{finite quadratic module } (A, q)) \quad \rightsquigarrow \quad \mathcal{C}(K, \mathfrak{n}, q),$$

i.e. from BC cyclotomic data to a pointed MTC with *explicit* modular data (S, T). For $K = \mathbb{Q}(i)$ and $n = 4$ the primitive character χ_4 (mod 4) yields the Gaussian phase i, exactly the semion topological spin; the modulus $n = 4$ corresponds to the Gaussian unit group and reduction $\mathcal{O}_{\mathbb{Q}(i)}/(2)$ gives $A \simeq \mathbb{Z}_2$. Thus the BC cyclotomic sector naturally *lands* on the Gaussian semion MTC.

Elliptic/Heegner sector as a coherence selector.

For a modular elliptic curve $E/\mathbb{Q}$ and an imaginary quadratic field $K = \mathbb{Q}(\sqrt{D})$ (Heegner hypothesis), Gross–Zagier gives

$$L'(E, 1) = \frac{C(E, K)}{\Omega_E} \frac{\widehat{h}(P_K)}{\sqrt{|D|}}, \qquad Z_E \propto \frac{1}{L'(E, 1)} \propto \frac{\Omega_E \sqrt{|D|}}{C(E, K)\widehat{h}(P_K)}.$$

We interpret Z_E as a *coherence weight* on moduli: states minimizing the Heegner height (e.g. class number one fields such as $K = \mathbb{Q}(i)$) maximize Z_E. The combined measure

$$\boxed{\mathbb{P}_\beta(K, \mathfrak{n}, q) \;\propto\; \underbrace{(\mathrm{N}\mathfrak{n})^{-\beta}}_{\text{BC/KMS (adeles/ideles)}} \;\times\; \underbrace{Z_E}_{\text{elliptic coherence}}}$$

defines a thermodynamic–coherent *stack* of arithmetic MTCs $\{\mathcal{C}(K, \mathfrak{n}, q)\}$, with $K = \mathbb{Q}(i)$ and small $\mathfrak{n}$ (e.g. (2)) singled out as the *Gaussian semion phase* ($c = 1$).

Weil representation, modularity, and physics.

The modular action on (A, q) is the finite *Weil representation* of $\mathrm{SL}_2(\mathbb{Z})$; the S-matrix is a finite Fourier transform on the finite adelic component, while T encodes the arithmetic quadratic phase. This gives a concrete, computable MTC at each $(K, \mathfrak{n}, q)$, with central charge determined by the Gauss sum. In our setting: (i) the cyclotomic BC sector (adeles/ideles, KMS) supplies *temperature/resolution* over levels; (ii) the elliptic Heegner sector (Gross–Zagier) supplies *coherence* (free energy); (iii) the Gaussian Heegner field selects the *semion* ($U(1)_2 \cong SU(2)_1$) as the minimal arithmetic MTC consistent with microtubular symmetry (rectangular $Q(i)$). Together they provide a number-theoretic modular substrate for the resonance mechanism proposed in this paper.

Appendix A.6. Adelic and Hecke Interpretation of the Combined Measure

The weight $(\mathrm{N}\mathfrak{n})^{-\beta}$ introduced in A.5 admits a canonical adelic origin. When combined with the elliptic coherence factor Z_E, it leads to a non–ad hoc, first–principles expression for the joint measure $\mathbb{P}_\beta(K, \mathfrak{n}, q)$ in terms of ideles, adeles, and Hecke characters. This setting unifies the Bost–Connes thermal dynamics of cyclotomic time perception with the elliptic modular geometry of Heegner coherence.

Adeles, ideles, and the norm character.

Let K be a number field and $\mathbb{A}_K^{\times}$ its ideles. The global norm $|\cdot|_K : \mathbb{A}_K^{\times} \to \mathbb{R}_{>0}$ is the product of local absolute values. For a finite idele $\mathbf{a}$ representing an integral ideal $\mathfrak{n} \subset \mathcal{O}_K$, the relation $|\mathbf{a}|_K^{-1} = \mathrm{N}(\mathfrak{n})$ identifies the factor $(\mathrm{N}\mathfrak{n})^{-\beta}$ with the adelic norm character $|\mathbf{a}|_K^{-\beta}$. This is precisely the weight entering the Bost–Connes C^*–dynamical system $(\mathcal{A}_{\mathbb{Q}}, \sigma_t)$ whose partition function is $Z_{\mathrm{BC}}(\beta) = \zeta(\beta)$ [30].

Tate's global zeta integral.

Tate's thesis (1950) expresses the Dedekind zeta function of K as an integral over the idele class group $C_K = \mathbb{A}_K^\times / K^\times$:

$$\zeta_K(\beta) = \int_{C_K} |\mathbf{a}|_K^{-\beta} \, d^\times \mathbf{a} = \sum_{\mathfrak{n} \subset \mathcal{O}_K} (\mathrm{N}\mathfrak{n})^{-\beta}.$$

Each Euler factor $(1 - \mathrm{N}\mathfrak{p}^{-\beta})^{-1}$ corresponds to a local integration over $K_\mathfrak{p}^\times$. Hence the BC weight $(\mathrm{N}\mathfrak{n})^{-\beta}$ is the local Boltzmann factor of the adelic product representation of $\zeta_K(\beta)$.

Origin of the eigenvalues $a_\mathfrak{p}$ (modularity theorem) [32].

For an elliptic curve $E/\mathbb{Q}$ of conductor N_E, the modularity theorem associates a unique normalized newform $f_E(q) = \sum_{n \geq 1} a_n q^n$ of weight 2 and level N_E such that $T_p f_E = a_p f_E$ for all primes p. The Hecke eigenvalues a_p are simultaneously the Frobenius traces

$$a_p = p + 1 - \#E(\mathbb{F}_p),$$

satisfying the Hasse bound $|a_p| \leq 2\sqrt{p}$ and multiplicativity $a_{mn} = a_m a_n$ for $(m, n) = 1$. The local Euler factor of the L–function is

$$L_p(E, s) = (1 - a_p p^{-s} + p^{1-2s})^{-1},$$

whose inverse roots (α_p, β_p)—the *Satake parameters*—satisfy $\alpha_p + \beta_p = a_p$, $\alpha_p \beta_p = p$. These parameters encode the two local Frobenius eigenvalues on the ℓ–adic Tate module of E.

Hecke characters and the adelic lift.

In the adelic language, the modular form f_E corresponds to an automorphic representation $\pi_E = \bigotimes'_p \pi_p$ of $\mathrm{GL}_2(\mathbb{A}_\mathbb{Q})$, with local L–factors $L_p(E, s) = (1 - \alpha_p p^{-s})^{-1}(1 - \beta_p p^{-s})^{-1}$. For each prime ideal $\mathfrak{p}$ of a quadratic extension K above p, one defines the local Hecke character

$$\phi_E(\mathfrak{p}) = \alpha_p^{f_\mathfrak{p}} + \beta_p^{f_\mathfrak{p}},$$

where $f_\mathfrak{p}$ is the residue degree of $\mathfrak{p}$ over p. Extending multiplicatively gives $\phi_E(\mathfrak{n}) = \prod_{\mathfrak{p}^r \| \mathfrak{n}} (\alpha_\mathfrak{p}^r + \beta_\mathfrak{p}^r)$, yielding an adelic character $\phi_E : \mathbb{A}_K^\times / K^\times \to \mathbb{C}^\times$ that enters the Hecke L–series

$$L(E/K, s) = \int_{C_K} |\mathbf{a}|_K^{-s} \, \phi_E(\mathbf{a}) \, d^\times \mathbf{a} = \sum_{\mathfrak{n}} \frac{\phi_E(\mathfrak{n})}{(\mathrm{N}\mathfrak{n})^s}.$$

The coefficients $a_\mathfrak{p}$ are thus not ad hoc constants but the Frobenius eigenvalues of E and the eigenvalues of the Hecke operators acting on the associated modular form f_E.

Mixed Hecke–Bost–Connes zeta function.

Combining the BC norm character and the modular Hecke character yields the *mixed zeta function*

$$\Xi_{E/K}(\beta) = \int_{C_K} |\mathbf{a}|_K^{-\beta} \, \phi_E(\mathbf{a}) \, d^\times \mathbf{a} = \sum_{\mathfrak{n}} \frac{\phi_E(\mathfrak{n})}{(\mathrm{N}\mathfrak{n})^\beta},$$

interpolating between the Dedekind zeta ($\phi_E \equiv 1$) and the modular L–function of E/K. Normalization by $\Xi_{E/K}(\beta)$ defines a canonical probability distribution on ideals $\mathfrak{n}$,

$$\boxed{\mathbb{P}_\beta(K, \mathfrak{n}, q) = \frac{(\mathrm{N}\mathfrak{n})^{-\beta} \, \phi_E(\mathfrak{n})}{\Xi_{E/K}(\beta)}.}$$

This distribution coincides with the expectation value of the BC KMS state twisted by the modular character ϕ_E.

Satake parameters as anyonic phase rotations.

In the arithmetic modular tensor category $\mathcal{C}(K, \mathfrak{n}, q)$ of A.5, the simple objects correspond to equivalence classes in $A = \mathcal{O}_K/\mathfrak{n}$ with topological spins $\theta_a = e^{2\pi i q(a)}$. At the adelic level, each prime $\mathfrak{p}$ contributes a local two–dimensional representation with eigenvalues $(\alpha_\mathfrak{p}, \beta_\mathfrak{p})$, which can be viewed as phase rotations of a pair of conjugate anyons. Indeed,

$$\alpha_\mathfrak{p} = p^{1/2} e^{+i\vartheta_\mathfrak{p}}, \qquad \beta_\mathfrak{p} = p^{1/2} e^{-i\vartheta_\mathfrak{p}},$$

with $\cos\vartheta_\mathfrak{p} = a_p/(2\sqrt{p})$. The phase angles $\vartheta_\mathfrak{p}$ play the role of *anyon braiding phases*—each prime defines a local braid monodromy in the adelic product, and the global modular S–matrix arises as the Fourier transform over these phases. Consequently, the arithmetic spectrum of Frobenius angles $\{\vartheta_\mathfrak{p}\}$ forms the discrete anyon–like topological spectrum underlying the mixed Hecke–Bost–Connes zeta function.

Relation to Connes–Marcolli and the BC system.

In the adelic formulation of the Bost–Connes theory [30,31], the space of $\mathbb{Q}$–lattices is a stack over the idele class group, and the time evolution acts by the global norm. Our construction extends this by incorporating a Hecke twist ϕ_E, encoding modular–elliptic information. At $\beta = 1$ the KMS states of the BC sector correspond to embeddings of cyclotomic fields, while the Hecke twist selects Heegner fields K of minimal discriminant. The resulting joint adelic system thus provides a natural "quantum–statistical" background for the arithmetic modular tensor categories $\mathcal{C}(K, \mathfrak{n}, q)$: the BC thermal weight arises from adeles/ideles, and the elliptic coherence from the Frobenius–Hecke phases of the modular form—interpreted physically as anyon rotations within the Gaussian semion phase ($U(1)_2 \cong SU(2)_1$, central charge $c = 1$).

References

1. Hameroff, S.; Penrose, R. Orchestrated Reduction of Quantum Coherence in Brain Microtubules: The Orch OR Model for Consciousness. *Philos. Trans. R. Soc. A* **1998**, *356*, 1869–1896.
2. Penrose, R. *Shadows of the Mind: A Search for the Missing Science of Consciousness*; Oxford University Press: Oxford, UK, 1994.
3. Penrose, R.; Hameroff, S. Consciousness in the Universe: An Updated Review of the Orch OR Theory. *Phys. Life Rev.* **2014**, *11*, 39–78.
4. Nishiyama, H.; Ito, Y.; Shimizu, H. Parametric Resonance in Microtubules: Quantum Optical Behavior and Anesthetic Sensitivity. *Quantum Rep.* **2025**, *7*, 43.
5. Planat, M. From Fibonacci Anyons to B-DNA and Microtubules via Elliptic Curves. *Quantum Rep.* **2025**, *7*, 49.
6. Nogales, E.; Whittaker, M.; Milligan, R.A.; Downing, K.H. High-Resolution Model of the Microtubule. *Cell* **1999**, *96*, 79–88.
7. Pampaloni, F.; Lattanzi, G.; Jon–, A.; Surrey, T.; Frey, E.; Florin, E.-L. Thermal Fluctuations of Grafted Microtubules Provide Evidence of a Length-Dependent Persistence Length. *Proc. Natl. Acad. Sci. USA* **2006**, *103*, 10248–10253.
8. Krivo-udsk-, O.; Dr-ber, P.; Cifra, M. Resolving Controversy of Unusually High Refractive Index of Tubulin. *Europhysics Letters* **2017**, *117*, 38003.
9. Huelga, S.F.; Plenio, M.B. Vibrations, Quanta and Biology. *Contemp. Phys.* **2012**, *53*(4), 274–298.
10. Desai, A.; Mitchison, T.J. Microtubule Polymerization Dynamics. *Annu. Rev. Cell Dev. Biol.* **1999**, *15*, 83–117.
11. Grifoni, M.; Hartmann L.; Berchtold, S.; Hänggi, P. Quantum tunneling and stochastic resonance. *Phys. Rev. E* **1996**, *53*, 5890–5898.
12. Kalra, P.; Benny, A.; Travis, S. M.; Zizzi, E. A.; Morales-Sanchez, A.; Oblinsky, D. G.; Craddock, T. J.A; Hameroff, S. R.; MacIver, M. B.; Tuszyński, J. A. et al. Electronic Energy Migration in Microtubules. *ACS Cent. Sci* **2023**, *9*, 352–361.
13. Craddock, T.J.A.; Friesen, D.; Mane, J.; Hameroff, S.; Tuszy?ski, J. A. The Feasibility of Coherent Energy Transfer in Microtubules. *J. R. Soc. Interface* **2014**, *11*, 20140677.

14. Fr-hlich, H. Long-Range Coherence and Energy Storage in Biological Systems. *Int. J. Quantum Chem.* **1968**, *2*, 641–649.
15. Planat, M.; Lardet-Vieudrin, F.; Martin, G.; Dos Santos, S.; Marianneau, G. Frequency Stability Enhancement from Carrier-Envelope Resonance in a Surface Acoustic Wave Delay Line Oscillator. *J. Appl. Phys.* **1996**, *80*, 2509–2515.
16. Gross, B.; Zagier, D. Heegner Points and Derivatives of *L*-Series. *Invent. Math.* **1986**, *84*, 225–320.
17. Darmon, H. Rational Points on Modular Elliptic Curves. In *Modular Forms and Fermat's Last Theorem*; Cornell, G.; Silverman, J.; Stevens, G., Eds.; Springer: New York, NY, USA, 1997; pp. 129–157.
18. Birch, B.J.; Mazur, B.J. Heegner Points and the Birch–Swinnerton-Dyer Conjecture. *Contemp. Math.* **1994**, *165*, 13–45. American Mathematical Society: Providence, RI, USA.
19. Diósi, L. M odels for universal reduction of macroscopic quantum fluctuations. *Phys. Rev. A* **1989**, *40*, 1165–1174.
20. Davydov, A.S. Solitons and Energy Transfer along Protein Molecules. *J. Theor. Biol.* **1977**, *66*, 379–387.
21. Hagan, S.; Hameroff, S.R.; Tuszynski, J.A. Quantum Computation in Brain Microtubules: Decoherence and Biological Feasibility. *Phys. Rev. E* **2002**, *65*, 061901.
22. Srivastava, P.; Bahuguna, S.; Banerjee, J.P. Modelling Microtubules in the Brain as n-Qudit Quantum Hopfield Networks and Beyond. *arXiv* **2015**, arXiv:1505.00774 [quant-ph].
23. Wiest, M.C. A quantum microtubule substrate of consciousness is experimentally supported and solves the binding and epiphenomenalism problems. *Neurosci. Conscious.* **2025** *2025* (1), niaf011.
24. Khan S, Huang Y, Timucin D; ; Dacks, A.M.; Otten, M.L.; Ananthasubramaniam, A.; Wiest, M.C. Microtubule-Stabilizer Epothilone B Delays Anesthetic-Induced Unconsciousness in Rats *eNeuro* **2024**; *11*, ENEURO.0291-24.2024.
25. Babcock, N.S.; Montes-Cabrera, G.; Oberhofer, K.E.; Mgbam, P.; Hu, B.L.; Kreisbeck, C.; Vym?tal, J.; Tortschanoff, A.; -anda, F.; Dijkstra, A.G.; Ba-i?–i-ko, A.; Watts, A.; Jansen, T.L.C. Ultraviolet Superradiance from Mega-networks of Tryptophan in Biological Architectures. *J. Phys. Chem. B* **2024**, *128*, 4035–4046.
26. Craddock, T.J.A.; Hameroff, S.R. Consciousness, Cognition and the Neuronal Cytoskeleton: A New Paradigm Needed in Neuroscience. *Front. Mol. Neurosci.* **2022**, *15*, 869935.
27. D-az Palencia, J.L. Self-Organized Criticality and Quantum Coherence in Tubulin Networks under the Orch OR Theory. *Appl. Math.* **2025**, *5*(2), 132–149.
28. Tegmark, M. The Importance of Decoherence in Brain Processes. *Phys. Rev. E* **2000**, *61*, 4194–4206.
29. Planat, M. On the cyclotomic quantum algebra of time perception. *Neuroquantology* **2004**, *2*, 292–308.
30. A. Bost and A. Connes, *Hecke algebras, type III factors and phase transitions with spontaneous symmetry breaking in number theory*, *Selecta Math. (N.S.)* **1** (1995) 411–457.
31. A. Connes and M. Marcolli, *Noncommutative Geometry, Quantum Fields and Motives*, American Mathematical Society, 2008.
32. J. Tate, Fourier Analysis in Number Fields and Hecke's Zeta Functions, Princeton University, 1950. Reprinted in J. W. S. Cassels and A. Fr-hlich (eds.), Algebraic Number Theory, Academic Press, 1967.